Materials and Interfaces

Scilight

Review

Check for updates

High-Entropy Intermetallic Nanocrystals: Formation Principles, Synthetic Strategies, and Electrocatalytic Applications

Cheng-Yu Wu [1,†], Bo-Han Wu [1,†], and Tung-Han Yang [1,2,3,*]

[1] Department of Chemical Engineering, National Tsing Hua University, Hsinchu 300044, Taiwan
[2] College of Semiconductor Research, National Tsing Hua University, Hsinchu 300044, Taiwan
[3] High Entropy Materials Center, National Tsing Hua University, Hsinchu 300044, Taiwan
* Correspondence: tunghanyang@mx.nthu.edu.tw
† These authors contributed equally to this work.
Received: 13 April 2026; Revised: 18 May 2026; Accepted: 25 May 2026; Published: 27 May 2026

Abstract: High-entropy intermetallic (HEI) nanocrystals have recently emerged as a promising class of multicomponent catalysts that combine the compositional complexity of high-entropy alloys with the structural precision of ordered intermetallics. This unique combination offers new opportunities to regulate atomic arrangement, surface structure, and catalytic behavior beyond what is achievable in conventional alloys or disordered high-entropy systems. In this Review, we discuss HEI nanocrystals from the perspectives of formation principles, synthetic strategies, and catalytic applications. We first outline the thermodynamic and kinetic factors that govern ordering in multicomponent nanoscale systems, and then summarize the emerging synthetic approaches for controlling phase selection, atomic ordering, and surface structure. We next examine representative electrocatalytic applications and discuss how ordering, multielement interactions, and structural evolution collectively influence activity and stability. Finally, we highlight four critical directions for future research, including growth mechanisms, facet control, atomic-scale structural identification and interatomic interactions, and electrocatalytic mechanisms. We anticipate that deeper insights into ordering, surface structure, and catalytic mechanisms will further expand the potential of HEI nanocrystals for a wide range of catalytic applications.

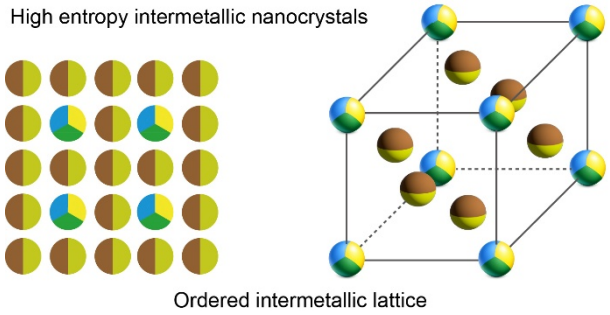

Keywords: high-entropy intermetallic nanocrystals; high-entropy alloy nanocrystals; atomic ordering; synthetic strategies; electrocatalysis

1. Introduction

High-entropy alloys (HEAs) have emerged as a distinctive class of multicomponent materials that extend alloy design beyond the conventional host-dominated framework [1,2]. In traditional alloys, one principal metal is typically modified by minor alloying additions to tailor structure and functionality. By contrast, HEAs are generally composed of multiple principal elements in near-equiatomic or comparable proportions, thereby creating a much broader compositional space and a more complex thermodynamic landscape [3–7]. This concept has opened access to metallic systems with unusual phase behavior, local atomic environments, and coupled physicochemical properties that are difficult to achieve in simpler alloys. Since their introduction, HEAs have attracted broad attention across materials science, initially for structural applications and more recently for energy-related and catalytic systems. The distinctive behavior of HEAs is often interpreted in terms of four core effects, namely the high-entropy effect, lattice distortion effect, sluggish diffusion effect, and cocktail effect [1,3,8]. The high-entropy effect refers to the configurational entropy contribution associated with multicomponent mixing, which can reduce the free energy of compositionally complex phases and, under appropriate conditions, favor

solid-solution formation. The lattice distortion effect arises from differences in atomic size, bonding characteristics, and electronic structure among constituent elements, leading to local strain and coordination heterogeneity. The sluggish diffusion effect describes the kinetically hindered atomic transport often observed in multielement systems, which can affect phase transformation and segregation behavior. The cocktail effect highlights that the overall functionality of a multicomponent alloy may differ substantially from a simple average of its individual constituents because emergent properties can arise from their collective interactions. Together, these effects provide a useful conceptual basis for understanding why HEAs often exhibit unusual combinations of structural stability, surface reactivity, and functional tunability.

With continued advances in nanoscale synthesis, the HEA concept has been successfully extended from bulk materials to HEA nanocrystals. This size reduction is not merely geometric. At the nanoscale, the high surface-to-volume ratio, the abundance of undercoordinated atoms, and the increased importance of surface and interface energetics make compositional and structural complexity even more consequential [9,10]. As a result, HEA nanocrystals have become highly attractive for catalysis, where surface atoms and their local environments largely determine reactivity. In these systems, multiple principal elements can generate a broad spectrum of adsorption sites with distinct coordination motifs and electronic structures, offering opportunities to simultaneously regulate activity, selectivity, and durability. Recent studies have therefore rapidly expanded the use of HEA nanocrystals in electrocatalysis, thermocatalysis, and photocatalysis [5,6,11–24]. Their promise lies not only in the ability to tune adsorption energetics and reaction pathways, but also in the possibility of discovering catalytic behaviors that cannot be readily accessed in monometallic or low-component alloy nanocrystals.

Despite this progress, most studies on HEA nanocrystals have focused on disordered solid-solution structures, in which constituent atoms are randomly distributed throughout the lattice. Although such disorder provides diverse local coordination and adsorption environments, it also limits precise control over atomic arrangement and active-site definition. In this context, high-entropy intermetallic (HEI) nanocrystals have recently emerged as a particularly intriguing direction because they introduce long-range atomic ordering into compositionally complex multielement systems [25–33]. Unlike disordered HEA nanocrystals, HEI nanocrystals combine multicomponent complexity with ordered crystallographic sublattices, enabling more defined site occupation, heteroatomic connectivity, and surface ensembles. This structural ordering is catalytically significant because it can provide more predictable local motifs and clearer correlations between atomic structure and catalytic function. Accordingly, HEI nanocrystals should not be regarded simply as ordered derivatives of HEA nanocrystals, but rather as a distinct class of nanoscale catalysts in which compositional complexity and crystallographic ordering coexist.

More importantly, atomic ordering can provide catalytic advantages that are difficult to achieve in disordered HEA nanocrystals. In disordered HEAs, the random distribution of elements generates a broad spectrum of local coordination environments, which is beneficial for creating diverse adsorption sites but may also obscure the relationship between atomic structure and catalytic function. By contrast, the ordered sublattices in HEI nanocrystals can produce more reproducible surface ensembles and better-defined active sites, enabling more systematic regulation of adsorption energetics and reaction pathways. Such ordering may also enhance catalytic selectivity by constraining the geometry of key intermediates and suppressing undesired adsorption configurations. In addition, stronger heteroatomic bonding and sublattice-specific coordination in ordered intermetallic frameworks can improve structural stability and mitigate elemental segregation or surface reconstruction under reaction conditions. Therefore, HEI nanocrystals offer a unique platform in which high-entropy compositional complexity and crystallographic ordering work together to optimize catalytic activity, selectivity, and durability.

In addition, the difference between HEI nanocrystals and conventional ordered intermetallic nanocrystals is equally significant. Traditional intermetallic compounds typically involve two or three elements arranged in ordered lattices with relatively fixed stoichiometry or narrow compositional windows. Their catalytic properties often arise from defined atomic ensembles, directional heteroatomic bonding, and characteristic electronic interactions. HEI nanocrystals retain the advantages of ordering while greatly expanding compositional complexity. By incorporating multiple principal elements into ordered frameworks, they offer a richer chemical landscape for tuning local coordination, charge distribution, and adsorption behavior. At the same time, they introduce a much more difficult ordering problem because several elements with distinct bonding preferences and site occupancies must be accommodated simultaneously. HEI nanocrystals thus represent a new frontier in which the structural precision of intermetallics intersects with the compositional versatility of high-entropy design.

Recent breakthroughs have demonstrated that ordered multicomponent nanocrystals can indeed be realized, highlighting the promise of HEI nanocrystals in catalysis [25–27,29–33]. Their ordered lattices can regulate local coordination geometry, orbital hybridization, and heteroatomic bonding in ways distinct from both conventional intermetallics and disordered HEA nanocrystals [30–32]. Nevertheless, the field remains at an early stage, and several key challenges remain unresolved. One major challenge is the formation of ordered HEI phases, because

configurational entropy tends to stabilize the disordered state, whereas ordering requires sufficient enthalpic driving force and accessible kinetic pathways for atomic rearrangement. At the nanoscale, this balance becomes even more complicated because particle size, surface energy, and diffusion limitations strongly influence phase evolution. Another challenge lies in synthetic control. Because several elements with different reduction behaviors, bonding preferences, and mobilities must be coordinated simultaneously, it remains difficult to reproducibly synthesize HEI nanocrystals with targeted compositions, uniform particle sizes, controlled morphologies, and well-defined ordering. In addition, the surface structure and catalytic roles of individual elements remain poorly understood. Even when bulk ordering is achieved, the active surface may deviate from the ideal lattice because of facet dependence, defects, local relaxation, or segregation. Under catalytic conditions, HEI nanocrystals may also undergo reconstruction or partial disordering, meaning that the catalytically relevant structure can differ substantially from the as-synthesized one.

In view of these opportunities and challenges, this Review focuses on HEI nanocrystals from the perspectives of formation principles, synthetic strategies, and catalytic applications. We first discuss the thermodynamic and kinetic foundations that govern ordering in multicomponent nanoscale systems and highlight how these principles differ from those of conventional alloys and simpler intermetallic nanocrystals. We then summarize the emerging synthetic approaches developed to access HEI nanocrystals, with emphasis on the key factors that control phase selection, atomic ordering, and surface structure. Next, we examine representative electrocatalytic applications and discuss how ordering, multielement interactions, and structural evolution collectively influence activity and stability. Finally, we highlight four critical directions for future research: growth mechanisms, facet control, atomic-scale structural identification and interatomic interactions, and electrocatalytic mechanisms. By integrating these aspects, this Review aims to provide a framework for understanding HEI nanocrystals and guiding the rational design of next-generation multicomponent catalysts.

2. Intermetallic Nanocrystals: Formation Principles, Synthetic Strategies, and Structural Advantages

Intermetallic nanocrystals are a structurally ordered class of materials that differ fundamentally from random alloy nanocrystals. Unlike disordered solid solutions, intermetallic phases exhibit long-range chemical ordering, in which constituent elements occupy specific crystallographic sublattices. Such atomic ordering modifies orbital hybridization and charge distribution, thereby tuning d-band characteristics, adsorption energetics, catalytic activity, selectivity, and stability [34–37]. The formation of intermetallic nanocrystals is governed by the interplay between thermodynamics and kinetics [38–40]. While negative mixing enthalpy associated with favorable heteroatomic bonding promotes ordering, configurational entropy and nanoscale surface energy tend to stabilize the disordered state. Achieving ordered structures therefore requires sufficient enthalpic driving force together with atomic diffusion within an appropriate temperature-time window. This chapter first introduces the thermodynamic and kinetic principles underlying intermetallic formation. It then discusses synthetic strategies including thermal annealing, rapid thermal shock, post-synthetic treatments, and epitaxial growth. Finally, the effects of atomic ordering on electronic structure and catalytic behavior are summarized.

2.1. Thermodynamic and Kinetic Framework for Intermetallic Nanocrystal Formation

The formation of ordered intermetallic nanocrystals from disordered alloys can be described within a coupled thermodynamic and kinetic framework, as illustrated in Figure 1a [38]. In thermodynamic terms, the free-energy landscape of a binary alloy features a metastable disordered state and a stable ordered intermetallic state separated by an energy barrier. The disorder-to-order transition is driven by the negative mixing enthalpy associated with favorable heteroatomic bonding, as specific atomic pairs in the ordered lattice maximize bond strength and coordination preference, thereby lowering the internal energy relative to the disordered state. The thermodynamic balance governing this transformation can be expressed as

$$\Delta G_{\mathrm{mix}} = \Delta H_{\mathrm{mix}} - T\Delta S_{\mathrm{mix}} \quad (1)$$

where ΔH_{mix} represents the enthalpic stabilization of ordered bonding and ΔS_{mix} denotes the configurational entropy contribution. During ordering, $\Delta H_{\mathrm{mix}} < 0$ due to strengthened heteroatomic interactions, while $\Delta S_{\mathrm{mix}} < 0$ because atomic positions become constrained to specific sublattices. Thus, ordering becomes thermodynamically favorable when the enthalpic gain outweighs the entropy penalty. However, at elevated temperatures, the $T\Delta S$ term increases, reducing the net driving force and stabilizing the disordered state. This competition defines a temperature-dependent thermodynamic driving force, here denoted as $F(T)$, which decreases with increasing temperature as entropy stabilization becomes dominant.

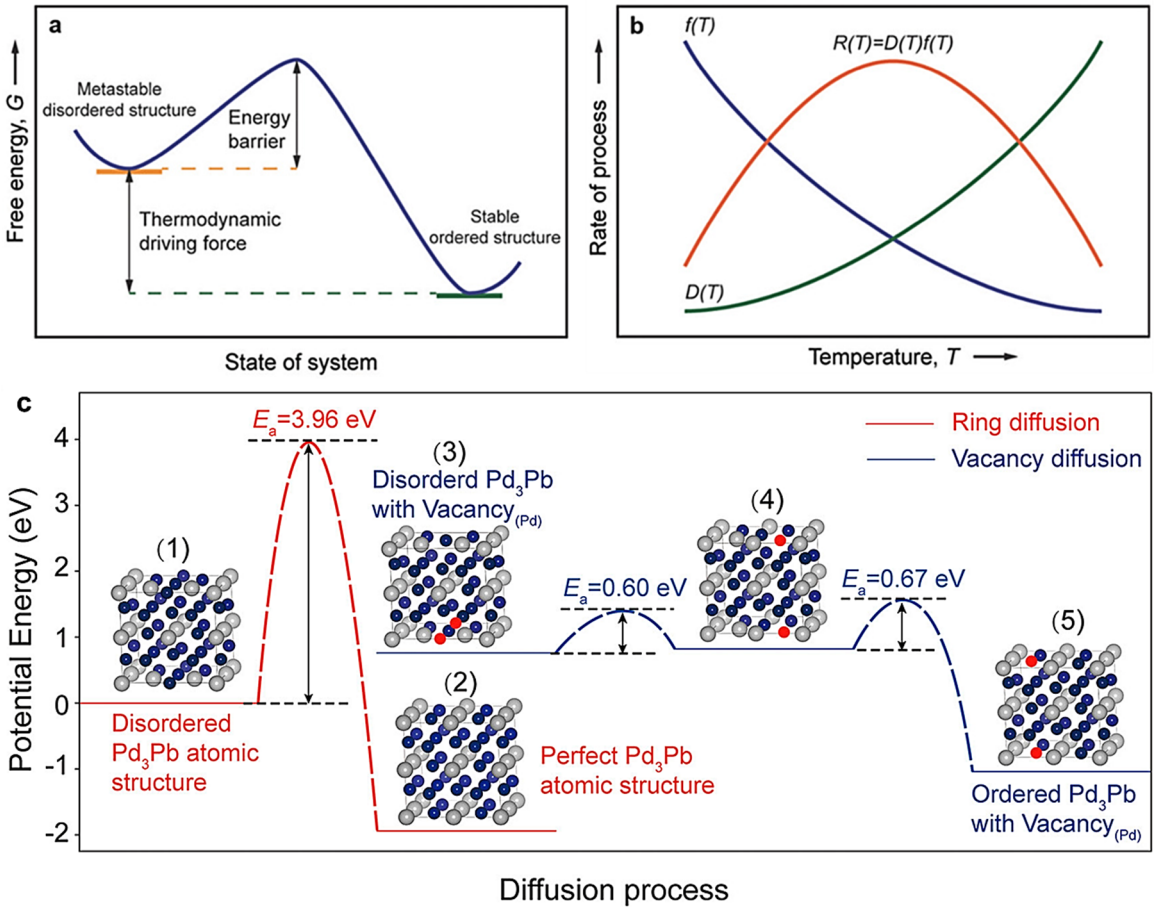

Figure 1. Thermodynamic and kinetic principles governing ordering in intermetallic systems. (**a**) Free-energy landscape illustrating the transformation from a metastable disordered structure to a stable ordered phase. (**b**) Temperature dependence of the ordering rate determined by the interplay between atomic diffusion and thermodynamic driving force. Reproduced with permission [38]. Copyright 2017, John Wiley and Sons. (**c**) Representative diffusion pathways during ordering in Pd_3Pb, comparing ring diffusion and vacancy-mediated diffusion. Reproduced with permission [40]. Copyright 2022, American Chemical Society.

At the nanoscale, surface energy contributions must also be incorporated into the free-energy description:

$$\Delta G = \Delta H_{\text{mix}} - T\Delta S_{\text{mix}} + \Delta\gamma A \tag{2}$$

where $\Delta\gamma$ is the difference in surface energy between ordered and disordered structures, and A is the particle surface area. Because surface atoms constitute a significant fraction of total atoms in nanocrystals, the $\Delta\gamma A$ term can substantially shift the effective disorder-order transition temperature. This size dependence can be estimated by

$$\frac{T_{\text{nano}}}{T_{\text{bulk}}} = 1 + \frac{A/V}{\Delta H_V}\Delta\gamma \tag{3}$$

where ΔH_V is the volume-specific enthalpy change and surface-to-volume ratio (A/V) scales inversely with particle size. As a result, surface energy effects become increasingly significant at the nanoscale, potentially destabilizing the ordered phase to the disordered state. Consequently, smaller nanocrystals may require more stringent thermal conditions to achieve ordering, even when the bulk phase is thermodynamically stable.

While thermodynamics defines the stability of the ordered state, the actual transformation pathway is governed by kinetics. The rate of the disorder-to-order transition can be expressed as

$$R(T) = D(T) \cdot F(T) \tag{4}$$

where $D(T)$ is the temperature-dependent diffusion coefficient and $F(T)$ represents the thermodynamic driving force defined above. As illustrated in Figure 1b [38], $D(T)$ increases exponentially with temperature due to enhanced atomic mobility, typically following an Arrhenius relationship:

$$D = D_0 \exp\left(-\frac{E_a}{RT}\right) \tag{5}$$

where E_a is the activation energy for diffusion. In contrast, $F(T)$ decreases with increasing temperature as entropy stabilization becomes significant. The product of these two competing factors results in a characteristic temperature window where $R(T)$ reaches a maximum, defining the optimal regime for intermetallic ordering. At low temperatures, the driving force for ordering may be strong, but atomic diffusion is kinetically limited. At excessively high temperatures, diffusion is rapid, but entropy suppresses the overall tendency toward ordering.

The atomistic diffusion mechanism governing the disorder-to-order transition is illustrated in Figure 1c using Pd_3Pb as a representative system [40]. Ordering requires long-range atomic rearrangement, which is primarily governed by atomic diffusion pathways. In ordered alloys, diffusion typically proceeds through two mechanisms: cooperative ring diffusion and vacancy-mediated diffusion. Ring diffusion involves the concerted displacement of multiple atoms and is therefore associated with a high activation barrier of about 3.96 eV. By contrast, vacancy-mediated diffusion has a much lower activation barrier of about 0.60–0.67 eV, enabling stepwise atomic exchange and the gradual development of long-range order. Vacancy-mediated diffusion therefore serves as the dominant kinetic pathway for disorder-to-order transformation in intermetallic nanocrystals. Nevertheless, sufficient thermal energy is still required to overcome migration barriers and activate atomic rearrangement. Taken together, the free-energy landscape of the disorder-to-order transition (Figure 1a), the temperature-dependent interplay between thermodynamic driving force and atomic diffusion (Figure 1b), and the atomistic diffusion pathways that enable atomic rearrangement (Figure 1c) collectively define the kinetic window for intermetallic nanocrystal formation. This coupled thermodynamic and kinetic framework explains why activation strategies such as high-temperature annealing and rapid thermal shock are often required to overcome diffusion barriers and promote long-range ordering. Representative synthetic approaches are discussed in the following sections.

2.2. Thermally Activated Routes to Intermetallic Nanocrystals

Building on the thermodynamic and kinetic framework discussed in Section 2.1, the synthesis of ordered intermetallic nanocrystals requires strategies that can overcome diffusion barriers and promote atomic rearrangement within nanoscale structures. In practice, such ordering can be achieved through several thermally activated routes, including rapid high-temperature activation, conventional annealing, diffusion-mediated phase evolution, and atomic reorganization revealed under in situ conditions. Because each approach regulates atomic mobility and thermodynamic driving force differently, they strongly influence particle size, ordering kinetics, and structural evolution. Representative examples are summarized in Figure 2, including rapid Joule heating and conventional annealing as thermally driven routes for intermetallic formation (Figure 2a), annealing-induced ordering pathways (Figure 2b), diffusion-controlled phase evolution (Figure 2c), and atomic-scale ordering mechanisms revealed by in situ electron microscopy (Figure 2d) [40–43].

One strategy for promoting rapid atomic ordering is ultrafast high-temperature activation. Rapid Joule heating has been demonstrated to synthesize intermetallic nanocrystals within extremely short time scales. By applying heating pulses to temperatures up to ~1600 K with ramp rates on the order of 10^5 K s^{-1}, disordered Pd-Pb precursors transform into ordered $L1_2$ Pd_3Pb nanocrystals within ~60 s (Figure 2a) [40]. Ultrafast heating generates a high concentration of vacancies in the transient alloy structure, markedly lowering diffusion barriers for atomic rearrangement. Density functional theory (DFT) calculations show that vacancy-mediated diffusion has a much lower activation energy than collective ring diffusion, thereby accelerating ordering. At the same time, the short thermal exposure suppresses particle coarsening and yields uniformly distributed nanocrystals of about 6 nm. In contrast, conventional furnace annealing at 1273 K can also produce ordered Pd_3Pb intermetallics, but prolonged heating typically results in much larger particles (~85 nm) due to enhanced coarsening. Despite this limitation, conventional annealing remains a widely used route to thermodynamically stable intermetallic phases because it provides sufficient atomic mobility for long-range ordering.

Under thermally activated conditions, conventional high-temperature annealing enables detailed observation of ordering pathways in alloy nanocrystals. In situ electron microscopy studies show that Pt-Fe alloy nanocrystals annealed at ~700 °C undergo a sequential ordering process (Figure 2b) [41]. The transformation begins with the rapid formation of an $L1_0$ PtFe surface layer, followed by conversion into an $L1_2$ Pt_3Fe phase that propagates inward. This process is governed by counter-diffusion of Pt and Fe atoms, where outward Pt diffusion and inward Fe diffusion drive compositional redistribution. Subsequent nucleation of the thermodynamically stable $L1_0$ PtFe phase in the particle core is followed by outward growth through the consumption of the surrounding Pt_3Fe region. The diffusion-mediated restructuring ultimately produces a PtFe@Pt core-shell configuration consisting of an $L1_0$ PtFe core and a thin Pt-rich shell. The respective high-resolution transmission electron microscope (HRTEM) image, representing the final diffusion-mediated state (iv) illustrated in Figure 2b, confirms the formation of the PtFe@Pt core-shell structure (Figure 2c).

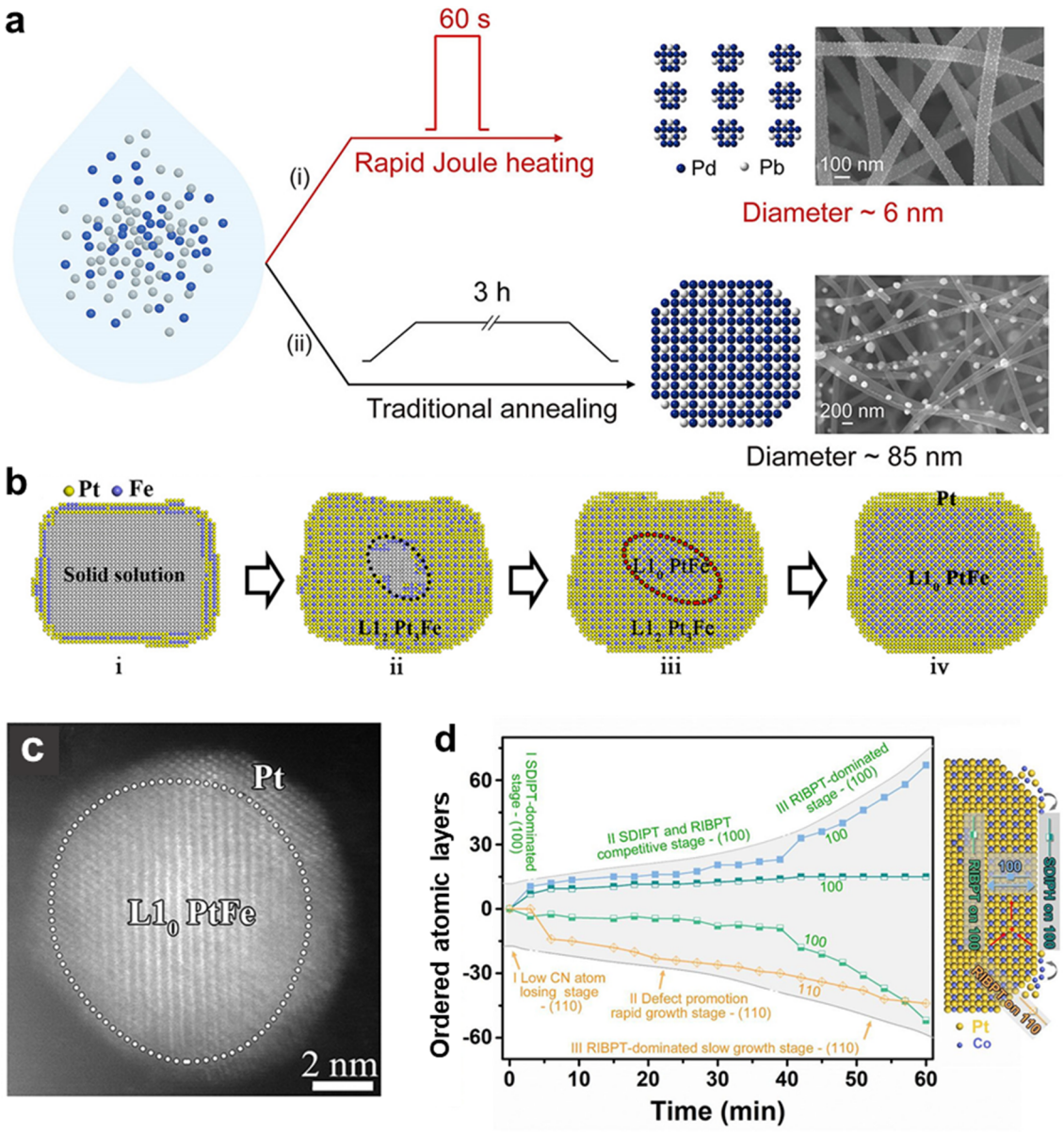

Figure 2. Representative thermally activated formation pathways of intermetallic nanocrystals. (**a**) Ultrafast ordering of Pd_3Pb nanocrystals via rapid Joule heating. Reproduced with permission [40]. Copyright 2022, American Chemical Society. (**b**,**c**) Thermally induced ordering pathway in Pt-Fe nanocrystals during annealing and HRTEM image of the well annealed PtFe@Pt core shell structure. Reproduced with permission [41]. Copyright 2022, PNAS. (**d**) In situ visualization of atomic ordering dynamics in Pt_3Co nanocrystals involving SDIPT and RIBPT mechanisms. Reproduced with permission [43]. Copyright 2021, American Chemical Society.

While high-temperature annealing enables thermodynamically driven ordering pathways (Figure 2b), intermetallic formation can also proceed through diffusion-controlled phase evolution when the migration of the second element is kinetically regulated [42]. In Pt-Sn systems, hydrogen reduction of $Pt/SnO_2@mSiO_2$ at moderate temperatures (~300 °C) enables controlled diffusion of Sn into Pt nanocrystals, leading to sequential phase transformations from Pt to Pt_3Sn and ultimately to PtSn. When the reduction time is limited to ~5 min, Sn diffusion remains incomplete, resulting in Pt_3Sn-enriched surfaces. Extending the reduction time to ~30 min produces Pt_3Sn/PtSn structures with coherent interfaces, whereas prolonged reduction (~4 h) leads to complete transformation into the PtSn intermetallic phase. These results highlight elemental diffusion control as an effective strategy for regulating phase evolution and structural development in intermetallic nanocrystals.

Beyond diffusion-controlled phase evolution, advanced in situ microscopy techniques have enabled direct visualization of atomic-scale ordering processes in intermetallic nanocrystals. In situ HRTEM studies of Pt_3Co nanocubes reveal that the transformation from a disordered face-centered cubic (FCC) alloy to an ordered $L1_2$ structure proceeds through two distinct mechanisms (Figure 2d) [43]. One pathway involves surface diffusion of

atoms from high-energy corner sites toward terrace regions, referred to as surface diffusion-induced phase transition (SDIPT). The other corresponds to reconstruction-induced body phase transition (RIBPT), where atomic rearrangement occurs within the nanocrystal interior through short-range reconstruction. The interaction between these processes governs the overall ordering dynamics and structural evolution of the nanocrystal, with surface diffusion dominating early stages and bulk reconstruction completing the ordering transformation.

Taken together, these representative studies show that the formation of ordered intermetallic nanocrystals is governed by the interplay between thermodynamic driving forces and kinetic pathways. Rapid thermal activation, conventional annealing, diffusion-mediated transformation, and atomic-scale reconstruction all demonstrate how atomic mobility, diffusion behavior, and defect formation regulate ordering dynamics and structural evolution in alloy nanocrystals. These findings are consistent with the framework described in Section 2.1, in which the accessible ordering window is determined by the balance between diffusion kinetics and thermodynamic driving force. Although the examples above mainly involve thermally activated processes, wet-chemical routes have also been developed to construct ordered intermetallic nanocrystals under solution-phase conditions. Representative solution-phase strategies are discussed in the following section.

2.3. Solution-Phase and Non-equilibrium Synthetic Strategies

In contrast to thermally driven approaches that rely on high-temperature diffusion to induce atomic ordering, solution-phase synthesis offers an alternative route for constructing ordered intermetallic nanostructures under milder conditions. Wet-chemical methods provide precise control over nucleation, precursor supply, and surface reactions, enabling the regulation of nanocrystal morphology, composition, and atomic distribution at the nanoscale [44–46]. These features are particularly advantageous for preserving well-defined nanostructures while introducing heteroatoms in a controlled manner.

A representative example is the seed-mediated synthesis of Cu@CuAu core-shell nanocubes, in which controlled precursor injection and interfacial diffusion enable the formation of single-atom-alloy (SAA) surfaces and ordered intermetallic shells [45]. In this system, Au precursors are introduced onto preformed Cu nanocubes, where galvanic replacement and atom interdiffusion driven by the Kirkendall effect leads to the initial dispersion of Au as isolated surface atoms, forming a dilute Cu@CuAu SAA structure. Increasing the Au precursor concentration induces further atomic rearrangement and ordering, resulting in the formation of a tetragonal CuAu intermetallic shell epitaxially grown on the Cu core. Atomic-resolution HAADF-STEM characterization reveals well-defined lattice features of the Cu core together with superlattice ordering in the CuAu shell, confirming the formation of the ordered intermetallic phase. Overall, solution-phase synthesis provides an effective route for regulating atomic distribution and interfacial ordering in nanoscale alloys under relatively mild conditions.

2.4. Structural Features and Catalytic Advantages of Intermetallic Nanocrystals

Beyond the synthetic approaches described above, the significance of intermetallic nanocrystals lies in their structurally defined atomic arrangements and the resulting catalytic advantages. Unlike random alloys, they exhibit long-range chemical ordering, in which constituent elements occupy specific crystallographic sublattices. This ordering creates well-defined coordination environments and surface ensembles, enabling systematic regulation of electronic structure, adsorption energetics, reaction pathways, and catalytic stability [47–49].

In this context, the catalytic behavior of multimetallic systems is commonly interpreted in terms of four fundamental effects: ligand, strain, geometric, and bifunctional effects (Figure 3a–d) [47]. When a second metal is introduced into a host metal lattice, the coordination environment of surface atoms is altered, leading to orbital hybridization and partial charge transfer between neighboring atoms. This electronic perturbation shifts the d-band center relative to the Fermi level and changes the adsorption strength of reaction intermediates, which is referred to as the ligand effect (Figure 3a). Lattice mismatch between different atomic layers can also generate tensile or compressive strain, thereby modifying interatomic distances and d-band dispersion and ultimately tuning adsorption energetics and catalytic activity (Figure 3b). In addition to these electronic effects, ordered intermetallic structures can influence catalytic behavior through geometric effects, in which constituent elements occupy specific lattice positions and form well-defined surface ensembles. Such arrangements can isolate active atoms or constrain adsorption configurations, thereby altering reaction pathways (Figure 3c). Furthermore, cooperative interactions between different metals may give rise to bifunctional mechanisms, in which one component preferentially adsorbs oxygen-containing species, such as OH*, that subsequently react with intermediates bound on neighboring sites. This cooperation lowers the energy barriers of key reaction steps and enhances catalytic performance (Figure 3d).

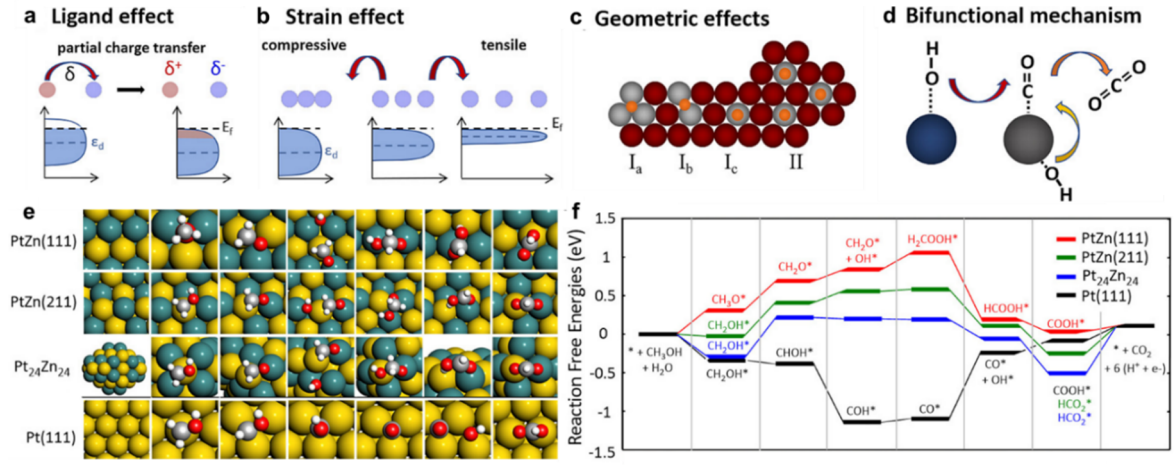

Figure 3. Structural and electronic factors governing catalysis in intermetallic nanocrystals. (**a**–**d**) Schematic illustrations of ligand, strain, geometric, and bifunctional effects. Reproduced with permission [47]. Copyright 2019, American Chemical Society. (**e**,**f**) Structure model and DFT-derived methanol oxidation pathways on PtZn and Pt surfaces. Reproduced with permission [49]. Copyright 2017, American Chemical Society.

These electronic and geometric effects can be further rationalized by DFT calculations. Projected density of states analysis reveals that alloying can significantly shift the d-band center relative to the Fermi level [48]. For example, incorporation of a second metal component causes the d-band center to downshift from −1.587 to −2.591 eV, indicating weakened metal-adsorbate interactions that facilitate the desorption of reaction intermediates. This electronic redistribution directly influences catalytic energetics. Consistent with this trend, free-energy calculations show that the ordered intermetallic structure exhibits a lower energy barrier for the potential-determining step than its disordered counterpart, suggesting more favorable reaction kinetics. These results highlight how heteroatomic coordination and structural ordering regulate electronic structure and adsorption energetics, thereby optimizing catalytic pathways.

Further insight into catalytic mechanisms can be gained by comparing DFT-derived reaction pathways (Figure 3e,f) [49]. For example, intermetallic PtZn preferentially follows a non-CO pathway during methanol oxidation, in which CH_2O* is converted into H_2COOH* through interaction with surface hydroxyl species before being further oxidized to CO_2. By contrast, pure Pt typically proceeds through a CO-mediated pathway involving CHOH*, COH*, and CO* intermediates. The strong stabilization of CO-related species on Pt creates a thermodynamic sink that hinders further oxidation and promotes catalyst deactivation through CO poisoning. In PtZn intermetallics, however, the presence of Zn modifies the adsorption environment and stabilizes surface hydroxyl species, thereby facilitating OH-assisted oxidation of intermediates and suppressing the formation of strongly bound CO species. As a result, intermetallic PtZn exhibits improved poisoning resistance and more favorable reaction energetics than pure Pt. In addition, site-dependent calculations suggest that undercoordinated surface atoms, such as corner and edge sites, can further lower the apparent reaction barriers, helping explain the enhanced catalytic activity often observed in intermetallic nanocrystals.

In addition to tuning adsorption energetics, structural ordering also enhances the stability of surface ensembles. In disordered alloys, local compositional fluctuations can promote surface segregation or atomic rearrangement under reaction conditions, leading to changes in active-site identity. By contrast, the periodic bonding network of intermetallic phases constrains atomic mobility through sublattice-specific coordination, thereby preserving structural integrity and well-defined active motifs during catalysis. Structural ordering therefore provides both electronic modulation and structural stability, reinforcing the structure-property relationships that distinguish intermetallic nanocrystals from random alloys. This understanding further motivates the extension of intermetallic design to compositionally complex high-entropy intermetallic nanocrystals, as discussed in the next section.

3. High-Entropy Intermetallic Nanocrystals: Formation Principles, Synthetic Strategies, and Experimental Realization

The extension from conventional intermetallic nanocrystals to multicomponent HEI nanocrystals introduces a much more complex ordering landscape. In HEIs, multiple principal elements participate simultaneously in lattice ordering, so configurational entropy, cooperative enthalpic interactions, and nanoscale effects collectively raise the thermodynamic threshold for ordered-phase formation [2,50–52]. Meanwhile, lattice distortion and

chemically heterogeneous local environments create distributed diffusion barriers, leading to more intricate and pathway-dependent atomic rearrangement than in binary intermetallic systems. HEI formation should therefore be understood as a multicomponent process governed by the interplay between thermodynamic stabilization and kinetic pathway selection. This chapter discusses the thermodynamic and kinetic design principles of HEIs and then summarizes the synthetic strategies and in situ characterization approaches that have enabled their formation and direct observation.

3.1. Thermodynamic and Kinetic Principles of HEI Nanocrystal Formation

While the thermodynamic and kinetic framework established for conventional intermetallic systems remains broadly applicable to multicomponent alloys, the presence of multiple principal elements substantially reshapes the energetic and structural landscape governing atomic ordering. The most immediate distinction arises from configurational entropy. For an N-component equiatomic alloy, the configurational entropy is given by

$$\Delta S_{\text{conf}} = R\ln\ N \tag{6}$$

which increases monotonically with the number of constituent elements. As illustrated in Figure 4, this entropy amplification significantly enlarges the $T\Delta S_{\text{conf}}$ contribution in the free-energy balance [2]. Although Figure 4 is presented in the context of mixing thermodynamics, the same configurational entropy term governs the stability of disordered states and thus directly influences the disorder-to-order transformation in multicomponent systems. In high-entropy systems, configurational entropy is the dominant entropy contribution and therefore represents the primary entropy term in the free-energy expression. Accordingly, the disorder-to-order transformation can be expressed as

$$\Delta G_{\text{ord}} = \Delta H_{\text{ord}} - T\Delta S_{\text{conf}} + \Delta\gamma A \tag{7}$$

where ΔH_{ord} represents the enthalpic stabilization associated with ordered bonding, while ΔH_{mix} describes the overall enthalpic tendency for multicomponent mixing relative to the pure elemental state (Equation (8)). The term $\Delta\gamma A$ accounts for surface energy contributions that become non-negligible at the nanoscale. Compared with binary intermetallic systems, the larger configurational entropy of multicomponent alloys more strongly stabilizes the disordered state. Consequently, HEI nanocrystal formation requires a sufficiently strong enthalpic driving force to overcome this entropy effect and enable ordering.

The formation of HEI nanocrystals is governed by the coupled effects of amplified configurational entropy, cooperative enthalpic stabilization, nanoscale size effects, and heterogeneous diffusion pathways [52]. Compared with conventional binary intermetallic systems, HEI formation proceeds under a significantly elevated thermodynamic threshold and follows a more complex structural evolution pathway. In multicomponent systems, achieving atomic ordering requires not only sufficiently negative ΔH_{mix} but also cooperative interactions among multiple elemental pairs, highlighting the critical role of compositional design in stabilizing ordered HEI phases.

This enthalpic contribution can be further quantified by expressing ΔH_{mix} as the summation of pairwise interaction enthalpies among constituent elements:

$$\Delta H_{\text{mix}} = \sum_{i\neq j} x_i\, x_j \Delta H_{ij} \tag{8}$$

where ΔH_{ij} denotes the mixing enthalpy between elemental pairs. As shown in Figure 5a, strongly negative ΔH_{ij} values favor chemical ordering, interactions with small magnitude stabilize entropy-dominated solid solutions, whereas positive values promote immiscibility and phase separation [2]. Unlike binary intermetallic systems, where a single strongly negative interaction may be sufficient to stabilize an ordered phase, HEI formation requires a cooperative enthalpic stabilization arising from multiple elemental pairs. In other words, long-range ordering can only emerge when the cumulative negative interactions collectively overcome the amplified configurational entropy. This requirement significantly narrows the compositional window capable of supporting HEI formation.

The two-dimensional interaction mapping therefore provides a practical guideline for compositional design (Figure 5b) [50]. By visualizing the enthalpic landscape, it becomes possible to identify element combinations in which dominant negative interactions promote ordering while minimizing strongly positive interactions that would otherwise drive phase separation. Importantly, the stability of HEIs is not dictated by a single pair interaction, but by the collective balance among all pairwise contributions. This cooperative enthalpic effect represents a defining characteristic of high-entropy systems and establishes a fundamental distinction from binary intermetallics, where ordering can often be traced to a single dominant interaction channel.

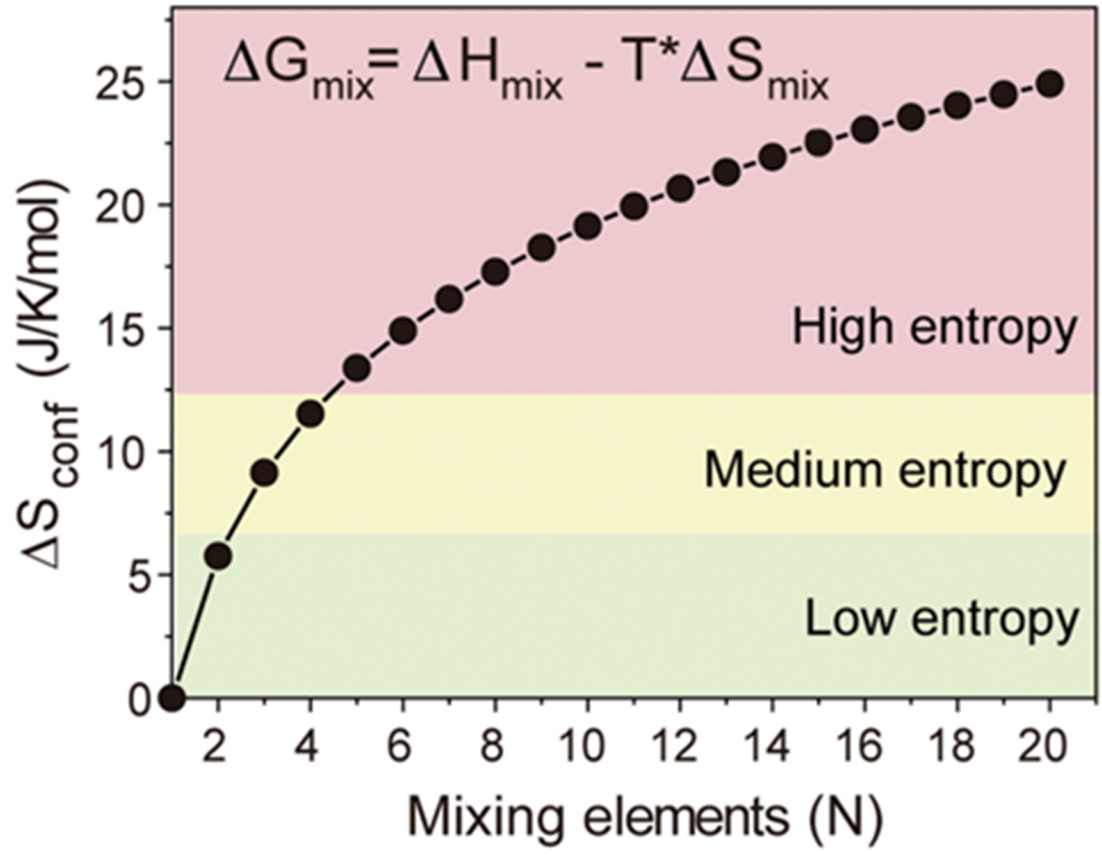

Figure 4. Configurational entropy (ΔS_{conf}) versus the number of mixing elements (N), highlighting the transition from low- to high-entropy regimes and its role in stabilizing HEIs. Reproduced with permission [2]. Copyright 2017, The American Association for the Advancement of Science.

Beyond thermodynamic elevation, the practical realization of HEIs is critically governed by kinetic pathway engineering, as illustrated in Figure 5c,d [2]. As described above, the ordering rate can be expressed by Equation (4), with the diffusion coefficient following an Arrhenius-type relationship:

$$D = D_0 \exp\left(-\frac{E_a^{eff}}{RT}\right) \tag{9}$$

In binary systems, atomic diffusion is usually governed by a relatively well-defined activation barrier, resulting in more predictable ordering behavior. By contrast, HEIs exhibit a distribution of migration barriers arising from lattice distortion and chemically heterogeneous local environments. Consequently, diffusion pathways become both spatially and elementally dependent, giving rise to a more complex kinetic landscape in which multiple metastable states may be accessed.

The rapid thermal shock pathway illustrated in Figure 5c shows how nonequilibrium processing can access entropy-stabilized structures in high-entropy systems. Ultrafast heating greatly enhances atomic mobility, enabling rapid elemental intermixing and the formation of a highly disordered state with maximized configurational entropy. Subsequent rapid quenching sharply suppresses long-range diffusion and freezes the atomic configuration, thereby kinetically trapping metastable states such as entropy-stabilized solid solutions or partially ordered structures, despite the thermodynamic driving force for ordering or phase separation. This decoupling between thermodynamic driving force and kinetic accessibility is particularly pronounced in high-entropy systems because of their intrinsically heterogeneous diffusion behavior. The temperature-time ordering diagram in Figure 5d further shows that structural evolution in HEIs is strongly governed by diffusion time. Rapid quenching preserves disordered or amorphous-like states by suppressing atomic rearrangement, whereas increasing diffusion time enables short-range ordering and the gradual emergence of intermetallic phases through vacancy-mediated diffusion. With further thermal exposure, long-range diffusion drives the system toward thermodynamic equilibrium and may ultimately lead to phase separation, depending on the enthalpic interaction landscape.

These results show that structural outcomes in HEIs are governed not only by thermodynamics but also by the extent of diffusion allowed during processing. The interplay between diffusion kinetics and thermodynamic

driving forces therefore determines structure selection across multiple metastable states, making kinetics a key design parameter in high-entropy systems. This pathway-dependent evolution distinguishes HEIs from conventional binary intermetallic nanocrystals and highlights the need for synthetic strategies that precisely control mixing, diffusion, and ordering.

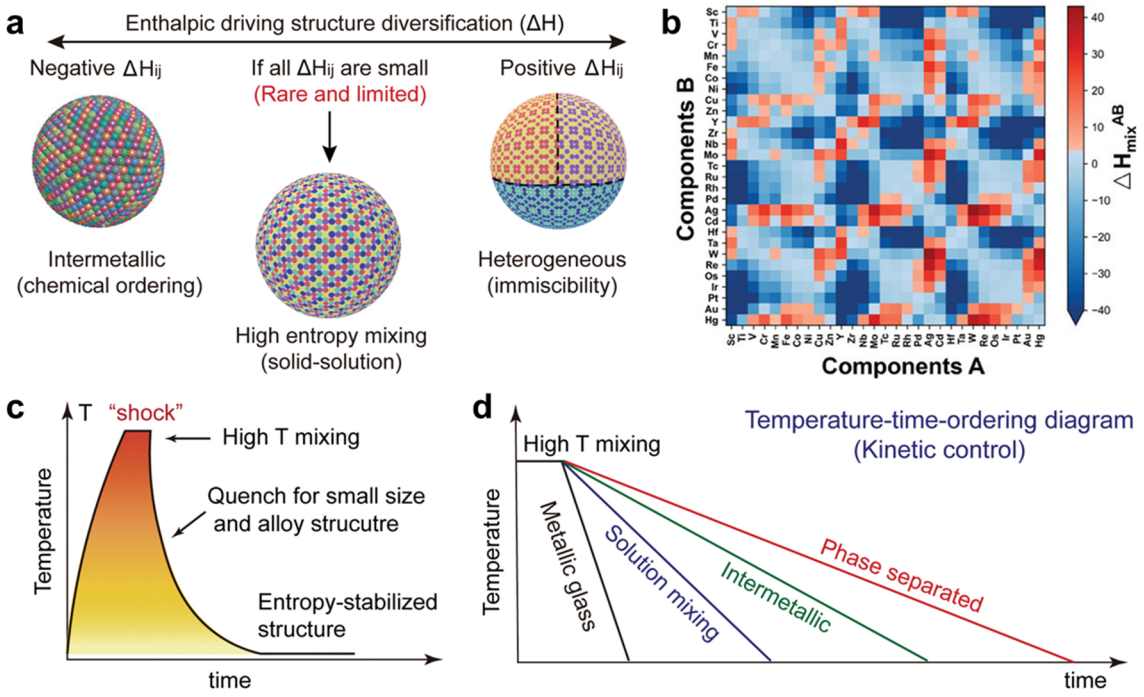

Figure 5. Enthalpic design and kinetic pathways in HEI formation. (**a**) Structure diversification determined by pairwise mixing enthalpy (ΔH_{ij}). (**b**) Pairwise interaction map (ΔH_{mix}AB). (**c**) Rapid thermal shock pathway. (**d**) Temperature-time ordering diagram illustrating kinetic selection among disordered, ordered, and phase-separated states. The images in (**a**,**c**,**d**) were reproduced with permission [2]. Copyright 2017, The American Association for the Advancement of Science. The image in (**b**) was reproduced with permission [50]. Copyright 2024, John Wiley and Sons.

3.2. Synthetic Strategies of HEI Nanocrystals

This section discusses the synthetic strategies and mechanistic understanding of HEI formation, with emphasis on the interplay between thermodynamics and kinetics in multicomponent systems. Unlike conventional intermetallics, HEI formation requires not only homogeneous mixing of multiple elements but also controlled atomic ordering within a limited kinetic window. Accordingly, several synthetic routes have been developed, including direct thermally driven HEI formation, thermally driven HEA-to-HEI conversion, and solution-phase synthesis [17,19,53–57]. In parallel, advanced in situ characterization techniques provide direct insight into the dynamic structural evolution during HEI formation, revealing temperature-dependent transitions from disordered solid solutions to ordered intermetallic phases and, ultimately, phase-separated states. These findings show that HEI formation is governed by kinetically accessible pathways rather than equilibrium thermodynamics alone, providing a framework for understanding and designing multicomponent intermetallic nanostructures.

3.2.1. Direct Thermally Driven Synthesis of HEI Nanocrystals

In multicomponent systems, direct thermally driven HEI formation typically involves high-temperature reduction of metal precursors followed by annealing to activate atomic diffusion and promote ordering. However, these conditions also accelerate particle sintering, causing coarsening and loss of active surface area. Excessive particle growth can further disrupt diffusion pathways and hinder atomic rearrangement, making direct HEI formation at the nanoscale more difficult. Strategies that suppress sintering while preserving sufficient atomic mobility are therefore essential. A representative strategy uses sulfur-anchored carbon supports to stabilize intermetallic nanocrystals during high-temperature ordering [17]. As illustrated in Figure 6a, metal precursors are first immobilized on sulfur-doped carbon through wet impregnation, followed by high-temperature H_2 reduction at 800–1100 °C. The strong metal-sulfur interaction anchors metal species and suppresses particle migration,

coalescence, and Ostwald ripening during thermal treatment. As a result, atomically ordered intermetallic nanocrystals smaller than 5 nm can be obtained even under conditions that would normally induce severe sintering. X-ray diffraction (XRD) and atomic-resolution imaging further confirm the formation of ordered intermetallic phases through characteristic superlattice reflections and well-defined atomic arrangements (Figure 6b–d). These results show that particle-size control is not only important for suppressing sintering, but also critical for balancing diffusion kinetics and thermodynamic stability during intermetallic formation at the nanoscale.

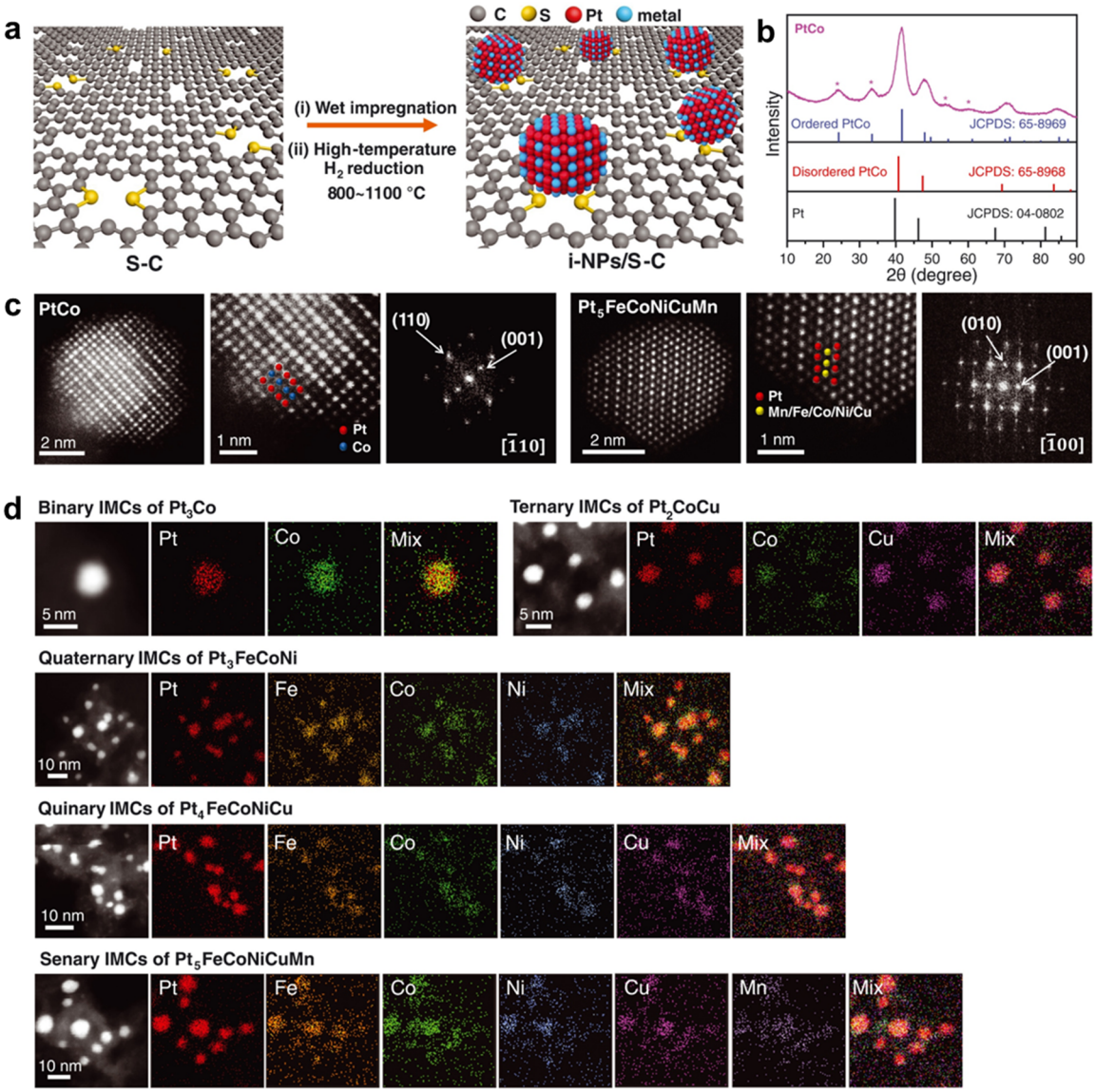

Figure 6. Direct thermally driven synthesis of HEI nanocrystals on sulfur-doped carbon supports. (**a**) Schematic of wet impregnation and high-temperature H_2 reduction on sulfur-doped carbon (S-C). (**b**) XRD patterns showing superlattice reflections of ordered intermetallic phases. (**c**) Atomic-resolution HAADF-STEM images and fast fourier transform (FFT) patterns confirming ordered structures. (**d**) Energy-dispersive X-ray spectroscopy (EDS) elemental maps demonstrating homogeneous distribution of multiple elements. Reproduced with permission [17]. Copyright 2021, The American Association for the Advancement of Science.

To elucidate the formation pathway of ordered intermetallics during annealing, temperature-resolved characterization provides direct and quantitative insight into both structural and chemical evolution [53,54]. In the hollow-carbon confinement system (Figure 7a–c), X-ray absorption near edge structure (XANES) and extended X-ray absorption fine structure (EXAFS) analysis shows a clear coordination transition, where Pt-N/O coordination decreases from 6.0 to 0, accompanied by the formation of Pt-Pt/Pt-TM bonds with coordination numbers of ~3–5, indicating reduction of metal precursors and the emergence of metallic bonding [53]. Consistent with this evolution, XRD shows the formation of an FCC alloy phase at intermediate temperatures between 500 and 700 °C, followed by the appearance of superlattice reflections such as (100) and (110) at 1000 °C, confirming the transition from a disordered alloy to an ordered intermetallic structure. More direct mechanistic evidence is

obtained from quasi-simultaneous in situ PXRD/XANES measurements (Figure 7d,e), where noble metals (Pt, Pd) reduce rapidly within ~150–175 °C, while 3d elements reduce gradually via intermediate states (~100–300 °C) [54]. This asynchronous reduction is reflected in the reduced metal fraction and correlates with the emergence of the FCC phase (~150–200 °C), followed by continuous lattice contraction from ~3.90 to ~3.76–3.80 Å due to progressive incorporation of smaller 3d elements. Together, these results reveal a stepwise formation mechanism in which rapid noble-metal reduction initiates nucleation, incorporation of 3d elements promotes compositional homogenization, and further thermal activation drives atomic ordering into intermetallic phases. This also highlights the unique power of in situ techniques to capture transient intermediates and kinetic pathways that cannot be resolved by ex situ analysis.

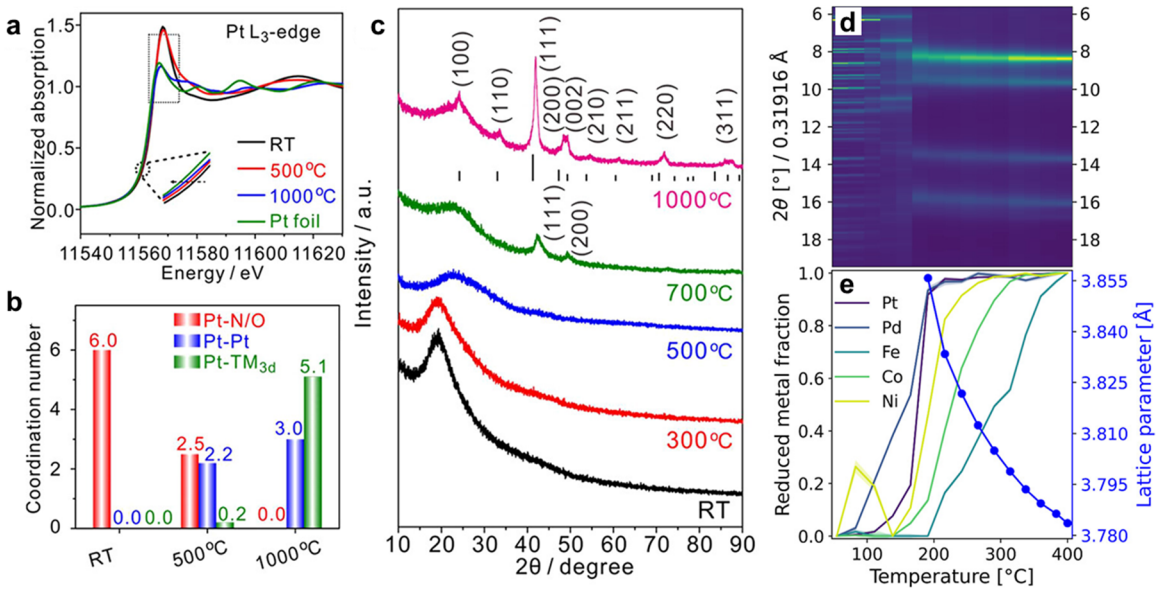

Figure 7. Temperature-resolved evolution of coordination, phase structure, and reduction behavior during HEI formation. (**a**) In situ Pt L_3-edge XANES. (**b**) EXAFS-derived coordination numbers showing Pt-N/O to Pt-Pt/Pt-TM transition. (**c**) XRD patterns indicating FCC formation between 500–700 °C and ordering at 1000 °C. Reproduced with permission [53]. Copyright 2023, American Chemical Society. (**d**) In situ PXRD contour plot. (**e**) Reduced metal fraction and lattice parameter evolution, revealing asynchronous reduction and lattice contraction. Reproduced with permission [54]. Copyright 2025, American Chemical Society.

3.2.2. Thermally Driven HEA-to-HEI Conversion

A representative route for thermally driven HEA-to-HEI conversion is to decouple the reduction of metal precursors and the nucleation and growth of HEA nanocrystals from the subsequent atomic ordering process [19]. As illustrated in Figure 8a,b, ultrafast Joule heating first generates chemically homogeneous HEA nanocrystals, after which a time-limited annealing step drives the disorder-to-order transition into a multiprincipal-element intermetallic phase (MPEI), followed by rapid cooling to preserve the ordered nanostructure. This two-step process sequentially addresses two key challenges: establishing uniform atomic mixing among multiple principal elements and enabling long-range ordering without severe particle coarsening or phase separation. Compared with conventional annealing, brief and controlled thermal exposure provides a practical route for converting HEAs into ordered HEIs while retaining ultrasmall particle size.

The structural evolution shown in Figure 8c,d further confirms the success of this approach. In the quinary $Pt(Fe_{0.7}Co_{0.1}Ni_{0.1}Cu_{0.1})$ system, aberration-corrected HAADF-STEM and elemental mapping reveal the coexistence of long-range atomic ordering and homogeneous multielemental distribution (Figure 8c), while the emergence and progressive sharpening of superlattice reflections in XRD demonstrate the continuous conversion from a disordered HEA precursor to an ordered intermetallic phase as annealing time increases (Figure 8d). These results are particularly important for HEI synthesis because they show that ordering can be achieved without sacrificing multicomponent compositional uniformity, which is often the major difficulty in extending intermetallic design beyond binary or ternary systems.

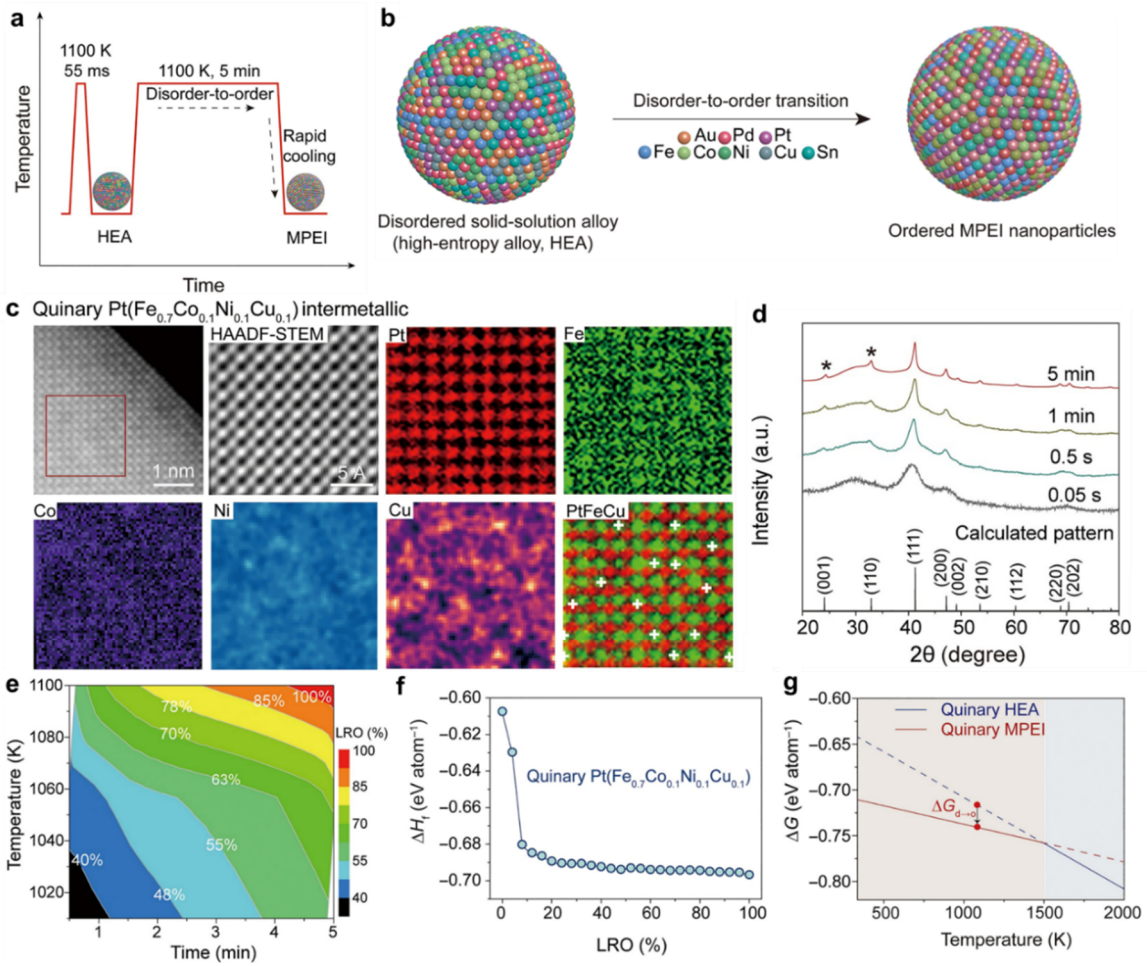

Figure 8. Rapid Joule heating enabled thermally driven HEA-to-HEI conversion. (**a**) Schematic illustration of the two-step thermal process consisting of rapid Joule heating and subsequent annealing. (**b**) Atomic transition from a disordered HEA to an ordered MPEI structure. (**c**) HAADF-STEM image and corresponding elemental maps of quinary $Pt(Fe_{0.7}Co_{0.1}Ni_{0.1}Cu_{0.1})$ intermetallic nanocrystals. (**d**) Time-resolved XRD patterns showing the evolution of superlattice peaks during annealing. (**e**) Temperature-time contour map of LRO. (**f**) Relationship between enthalpy change and ordering degree. (**g**) Temperature-dependent Gibbs free energy profiles of the HEA and MPEI phases. Reproduced with permission [19]. Copyright 2022, The American Association for the Advancement of Science.

This case provides direct experimental support for the coupled thermodynamic and kinetic framework of HEI formation. The successful formation of an ordered quinary intermetallic phase indicates that the cumulative enthalpic stabilization among multiple elemental pairs can overcome the amplified configurational entropy that stabilizes the disordered HEA phase. The temperature-time contour map of long-range ordering (LRO) (Figure 8e) further reveals a well-defined processing window, in which increasing temperature and dwell time enhance atomic diffusion and promote ordering, highlighting the importance of kinetic accessibility. Consistently, the monotonic decrease in enthalpy with increasing ordering degree (Figure 8f) confirms that the disorder-to-order transition is driven by cumulative enthalpic gain, while the calculated Gibbs free energy profiles (Figure 8g) show that the disordered HEA phase is favored at higher temperatures because of configurational entropy, whereas the ordered MPEI phase becomes more stable at lower temperatures where enthalpic stabilization dominates. Importantly, the ordered phase can only be retained when particle growth is effectively suppressed, whereas prolonged annealing leads to substantial coarsening and phase separation. These results show that successful HEI synthesis requires not only sufficient enthalpic driving force for ordering but also precise control of the thermal budget to balance atomic diffusion and structural stability. Accordingly, this work establishes a practical synthetic framework in which precursor homogenization, limited-time ordering, and rapid quenching are integrated to access ordered multicomponent intermetallic nanocrystals that are difficult to obtain under near-equilibrium conditions.

Constructing ordered multicomponent intermetallic nanocrystals via thermal annealing remains challenging due to concurrent particle coarsening, compositional segregation, and complex diffusion pathways in multicomponent systems. To address these challenges, a template-assisted thermal annealing strategy is employed, as illustrated in Figure 9a. PtCu nanosheets first serve as structural templates, enabling the incorporation of

additional metal species, such as Pd, Ag, Ru, and Fe, to form multicomponent nanosheets with homogeneous elemental distribution [55]. Subsequent annealing at elevated temperature (650 °C) induces atomic diffusion and rearrangement, leading to the transformation from disordered multicomponent nanosheets into structurally ordered intermetallic nanocrystals. TEM and HAADF-STEM analyses (Figure 9b–d) confirm that the nanocrystals maintain a uniform size (~5 nm) without obvious agglomeration after thermal treatment, indicating that the template effectively suppresses coarsening during ordering.

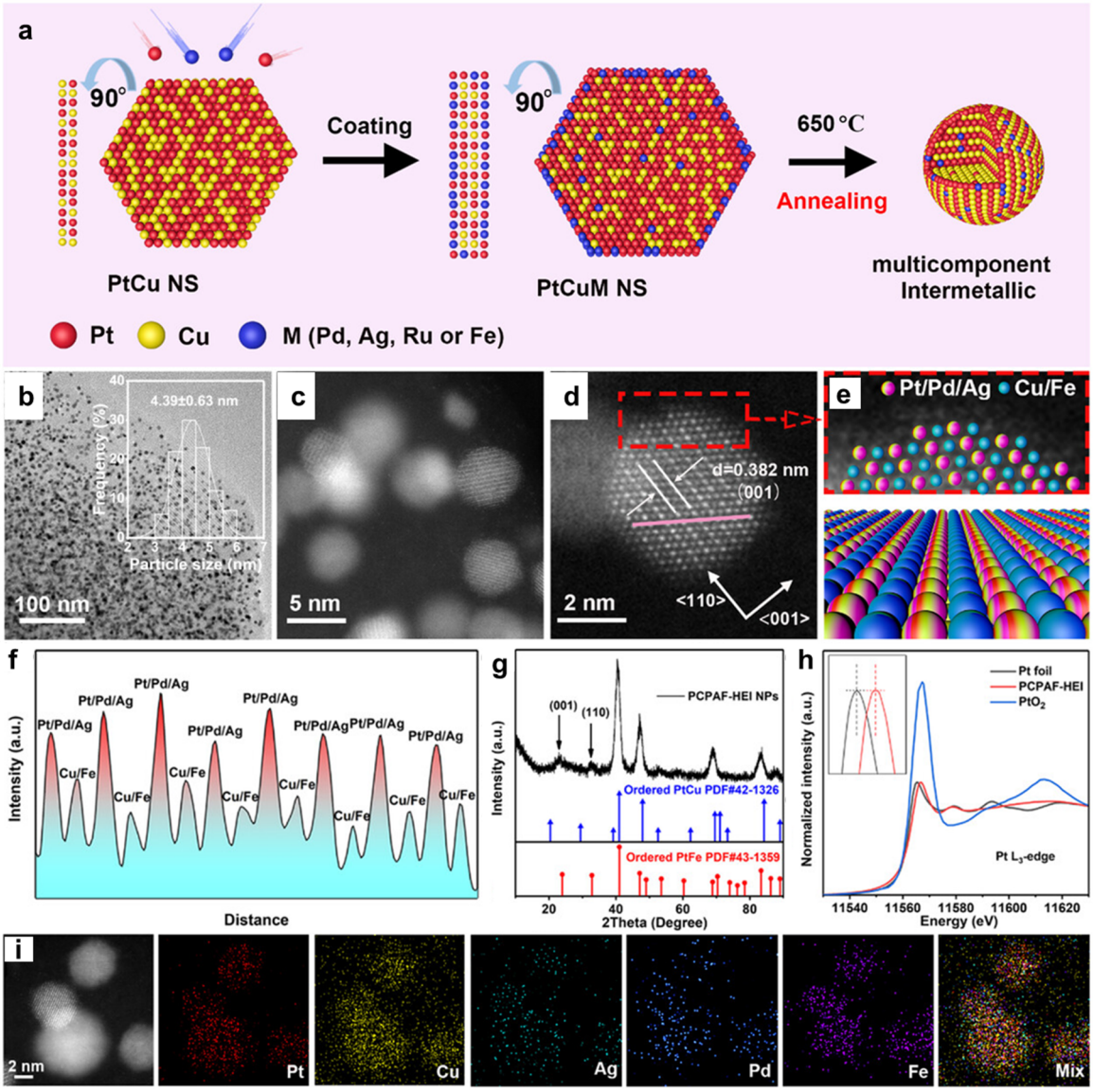

Figure 9. Template-assisted thermally driven HEA-to-HEI conversion and structural characterization of HEI nanocrystals. (**a**) Schematic illustration of the formation process of intermetallic nanocrystals. (**b**–**d**) TEM and HAADF-STEM images of nanocrystals. (**e**,**f**) Atomic-resolution HAADF-STEM and corresponding intensity profile revealing an ordered $L1_0$-type structure with alternating high-Z and low-Z atomic columns. (**g**) XRD pattern of ordered intermetallic phases, located between $L1_1$-PtCu and $L1_0$-PtFe. (**h**) Pt L_3-edge XAFS spectra. (**i**) STEM-EDS elemental mappings. Reproduced with permission [55]. Copyright 2024, John Wiley and Sons.

At the atomic scale, aberration-corrected HAADF-STEM reveals clear alternating contrast between high-Z (Pt/Pd/Ag) and low-Z (Cu/Fe) atomic columns along the <001> direction, consistent with the formation of a chemically ordered $L1_0$-type structure (Figure 9d,e). The corresponding intensity profile observed in HRTEM and XRD further verify the successful transition to intermetallic phases (Figure 9f,g). Notably, the introduction of Fe significantly alters the crystal structure, shifting from an $L1_1$-like PtCu-based phase to an $L1_0$-type structure resembling PtFe, as evidenced by both lattice fringe variation and XRD peak positions. This indicates that compositional modulation can effectively tune the final ordered phase through thermally activated atomic redistribution. X-ray absorption fine structure (XAFS) analysis further supports this structural evolution, where

the Pt L_3-edge white-line intensity remains close to that of metallic Pt and distinctly different from PtO_2, confirming that Pt maintains a metallic state after annealing (Figure 9h). Meanwhile, the observed shift in white-line features suggests a modification in the d-band electronic structure of Pt, indicative of electron redistribution among neighboring elements within the ordered lattice. Furthermore, elemental mapping and line-scan analyses confirm a uniform distribution of all constituent elements without phase segregation, suggesting that high-temperature annealing promotes not only ordering but also compositional homogenization (Figure 9i). Overall, this template-assisted thermally driven HEA-to-HEI conversion enables the controlled formation of multicomponent HEI nanocrystals with well-defined atomic ordering, tunable crystal structures, and corresponding electronic-structure modulation for tailored catalysis.

To further elucidate the thermally driven ordering pathway and phase stability, in situ HAADF-STEM is used to directly track the structural evolution of multicomponent PtRuFeCoNi HEA atomic layers on Pd nanocubes with {100} facets during annealing (Figure 10) [56]. Below 200 °C, the atomic layers retain a disordered FCC solid-solution structure with randomly distributed elements (Figure 10a–o). Upon heating to 300 and 400 °C, a progressive disorder-to-order transition occurs, leading to the emergence of $L1_0$ and subsequently $L1_2$ intermetallic phases, as evidenced by the appearance of characteristic superlattice reflections and atomic-scale intensity modulation (Figure 10p–y). This transformation is attributed to thermally activated interdiffusion between PGMs and IGMs, where the relatively faster inward diffusion of smaller IGM atoms induces sublattice rearrangement and ordering. Notably, further increasing the temperature to 500 °C results in phase separation, accompanied by morphological evolution from cubic to pseudospherical particles and the formation of a Pt-rich surface layer (Figure 10z–ad). FFT analysis reveals the coexistence of multiple phases, including FCC Pt, Pd, and $L1_2$ intermetallic domains, indicating the breakdown of the ordered structure at elevated temperature. These observations collectively reveal a temperature-dependent evolution from high-entropy solid solution to ordered intermetallic phases and ultimately to phase-separated states, highlighting that the ordered intermetallic structure formed during annealing represents a metastable state governed by kinetic constraints in this case (Figure 10ae,af).

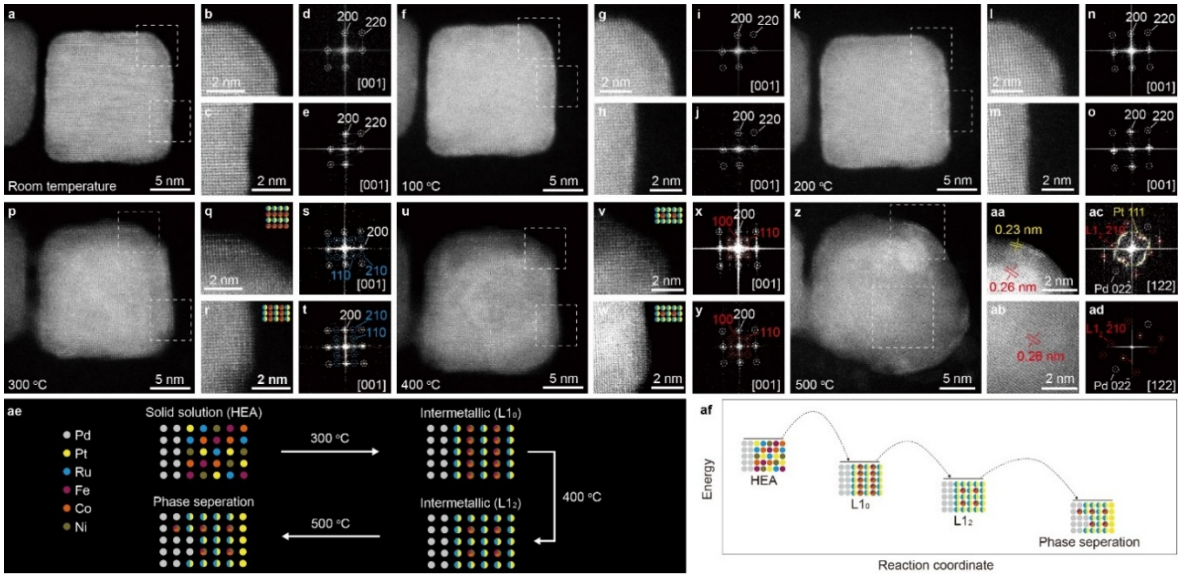

Figure 10. Temperature-dependent HEA-to-HEI conversion and metastability of multicomponent atomic layers revealed by in situ HAADF-STEM. HAADF-STEM images and corresponding FFT patterns of Pd@PtRuFeCoNi core-shell nanocubes at different temperatures: (**a**–**e**) room temperature, (**f**–**j**) 100 °C, (**k**–**o**) 200 °C, (**p**–**t**) 300 °C, (**u**–**y**) 400 °C, and (**z**–**ad**) 500 °C. (**ae**) Schematic illustration of the temperature-induced phase evolution from solid-solution PtRuFeCoNi atomic layers to ordered $L1_0$ and $L1_2$ intermetallic phases, followed by phase separation. (**af**) Schematic illustration highlighting the kinetically controlled nature of PtRuFeCoNi atomic layers as a metastable phase. Reproduced with permission [56]. Copyright 2024, The American Association for the Advancement of Science.

3.2.3. Solution-Phase Synthesis of HEI Nanocrystals

In contrast to thermally driven synthesis at elevated temperatures, direct solution-phase synthesis provides an alternative route for constructing intermetallic nanostructures under comparatively mild conditions. Although the reaction temperature is substantially lower, the formation of ordered intermetallic phases can still be achieved when sufficient atomic diffusion and rearrangement are enabled during crystal growth. A representative example

is the one-pot synthesis of PtRhBiSnSb HEI nanoplates at 220 °C, where the combined use of suitable precursors, coordinating solvents, surfactants, and reducing agents allows prolonged atomic exchange and structural reorganization in the solution phase [57]. Under these conditions, the product evolves into well-defined hexagonal nanoplates with a single-phase hcp structure, as confirmed by TEM and XRD analyses (Figure 11a–g). Aberration-corrected HAADF-STEM further reveals well-ordered atomic stacking along multiple zone axes, consistent with a hexagonal close packing (HCP) PtBi-type intermetallic framework. The measured lattice spacing and distinct atomic-column contrast indicate that the five constituent elements are incorporated into a chemically ordered lattice rather than a random solid solution. In addition, elemental mapping suggests a spatially regulated elemental distribution within the nanoplate, further reflecting that low-temperature wet-chemical synthesis can still support progressive atomic redistribution and ordering (Figure 11h). This example highlights that, beyond high-temperature annealing, intermetallic formation may also be realized through kinetically accessible diffusion pathways in solution, provide that crystal growth and atomic reorganization are sufficiently sustained.

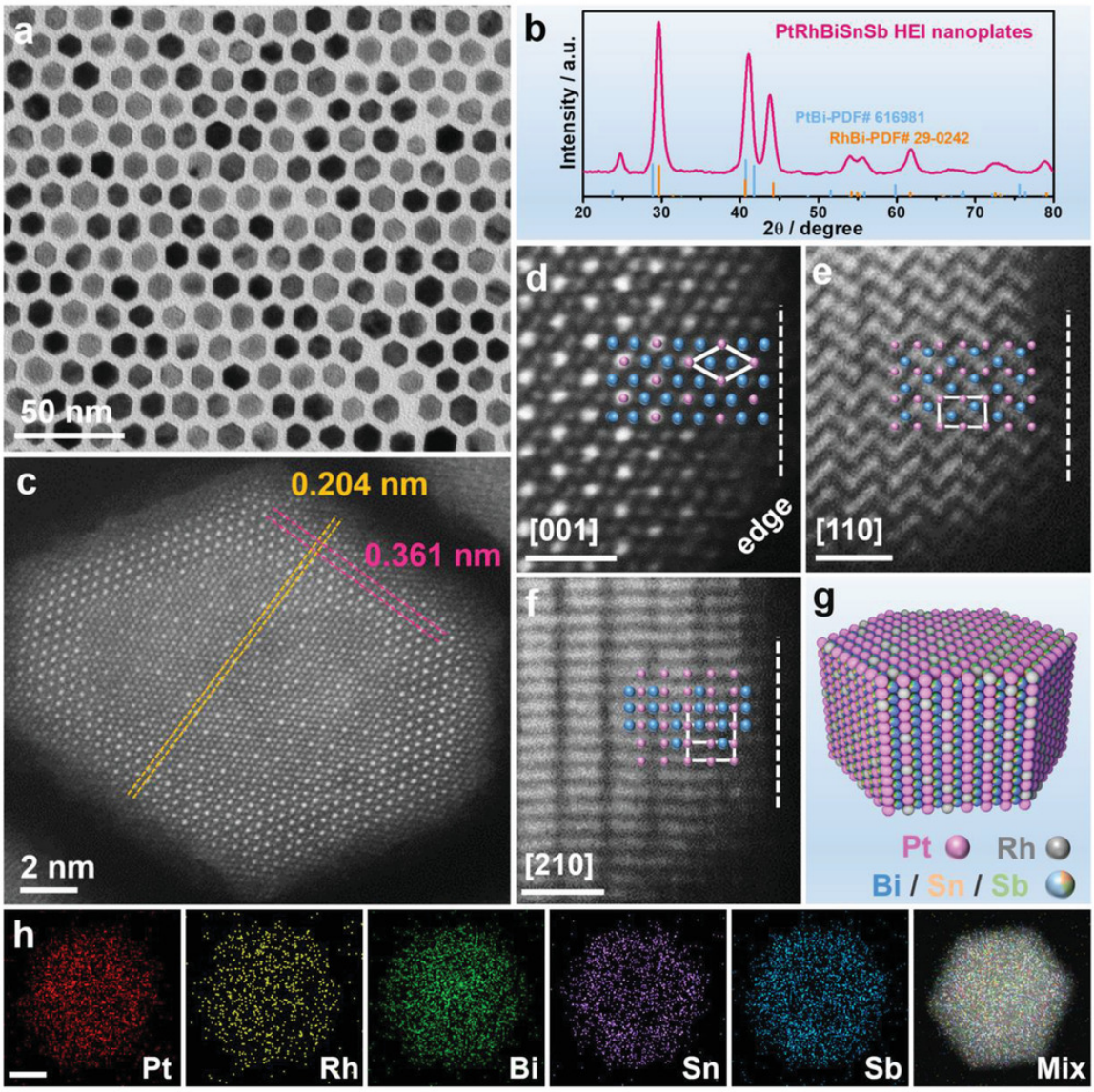

Figure 11. Solution-phase synthesis of HEI nanocrystals. (**a**) TEM image; (**b**) XRD pattern; and (**c**–**f**) Typical aberration-corrected HAADF-STEM images of the surface of PtRhBiSnSb HEI nanoplates. The insets in (**d**–**f**) show the corresponding PtBi unit cells viewed along different zoom axes. The pink and blue spheres represent Pt and Bi atoms, respectively. Scale bars: 1 nm. (**g**) The schematic illustration showing the atomic arrangement of Pt/Rh/Bi/Sn/Sb atoms on the surface of the PtRhBiSnSb HEI nanoplate. (**h**) EDS mapping images of a PtRhBiSnSb HEI nanoplate. Scale bar: 5 nm [57]. Reproduced with permission [57]. Copyright 2022, John Wiley and Sons.

Taken together, these three synthetic routes highlight that HEI nanocrystals can be accessed through distinct yet complementary pathways, including direct thermally driven synthesis, thermally driven HEA-to-HEI conversion, and solution-phase synthesis. Although these approaches differ in processing conditions, they share a

common requirement: the need to balance multielement mixing, atomic diffusion, and ordering within an appropriate kinetic window. Direct thermally driven synthesis relies on suppressing sintering while maintaining sufficient mobility for ordering, HEA-to-HEI conversion separates multicomponent mixing from subsequent ordering to improve structural control, and solution-phase synthesis offers a milder route in which crystal growth and atomic reorganization can proceed simultaneously. Together, these studies show that HEI formation is governed not only by thermodynamic driving forces but also, more importantly, by how synthetic pathways regulate diffusion, ordering, and structural stabilization across nonequilibrium conditions.

In summary, the three major synthetic routes to HEI nanocrystals exhibit complementary strengths and limitations. Direct thermally driven synthesis provides sufficient atomic mobility to achieve high ordering degree and thermodynamically stable intermetallic phases, but it often suffers from particle coarsening, sintering, and possible phase segregation, making particle-size control difficult without anchoring or confinement strategies. Thermally driven HEA-to-HEI conversion improves compositional homogeneity by separating multielement mixing from subsequent ordering, thereby offering better control over ordering evolution and phase purity. However, this approach is highly sensitive to thermal budget, because insufficient annealing causes incomplete ordering whereas excessive annealing may lead to coarsening or phase separation. Solution-phase synthesis offers superior control over particle size, morphology, and surface structure under milder conditions and can effectively suppress sintering, but the lower reaction temperature may limit atomic diffusion and ordering degree. In addition, precursor compatibility, ligand effects, phase purity, and large-scale reproducibility remain important challenges. The advantages and limitations of these representative synthetic strategies are comparatively summarized in Table 1, with emphasis on particle-size control, ordering degree, phase purity, sintering resistance, and scalability. Therefore, future HEI synthesis may benefit from combining the high ordering capability of thermal methods with the size, morphology, and surface control enabled by solution-phase approaches.

Table 1. Advantages and limitations of representative synthetic strategies for HEI nanocrystals.

Synthetic Strategy	Advantages	Limitations
Direct thermally driven synthesis	(1) High atomic mobility (2) High phase crystallinity (3) Access to thermodynamically stable phases	(1) Particle coarsening (2) Sintering (3) Possible phase segregation
Thermally driven HEA-to-HEI conversion	(1) Decouples multielement mixing and ordering (2) Improved phase purity and compositional homogeneity through separated mixing and ordering steps (3) Tunable ordering degree	(1) Sensitive to annealing temperature and time (2) Incomplete ordering if under-treated (3) Coarsening or phase separation if over-treated
Solution-phase synthesis	(1) Better morphology/size control (2) Reduced sintering (3) Suitable for shape and facet engineering (4) Milder reaction conditions	(1) Limited atomic diffusion (2) Ordering degree may be lower (3) Phase purity is sensitive to precursor reactivity and ligand coordination. (4) Large-scale reproducibility remains challenging

4. Electrocatalytic Applications of HEI Nanocrystals

As a structurally ordered class of multicomponent catalysts, HEI nanocrystals have opened new opportunities for electrocatalyst design because of their highly tunable electronic structures and unique ordered lattices. Unlike conventional binary intermetallic compounds and disordered HEA nanocrystals, HEI nanocrystals incorporate multiple elements into specific crystallographic sublattices, thereby generating well-defined atomic arrangements. Such structural features not only enable more precise isolation of active sites but also strengthen coordination interactions between noble and non-noble metals [58,59]. As a result, HEI nanocrystals can effectively regulate surface electronic structure and adsorption behavior, optimize the adsorption energetics of key reaction intermediates, and reduce competitive adsorption, thereby enhancing catalytic activity and selectivity [2]. Although catalytic studies of HEI nanocrystals remain less extensive than those of HEA nanocrystals, HEIs have already been explored in several important electrocatalytic reactions, such as the hydrogen evolution reaction (HER), oxygen reduction reaction (ORR), and ethanol oxidation reaction (EOR), as shown in Table 2. Existing studies have shown that HEI catalysts can exhibit higher activity and improved stability than conventional binary

intermetallic compounds or their corresponding HEA counterparts, highlighting the critical role of structural ordering in governing catalytic behavior. This chapter therefore reviews recent progress in the electrocatalytic applications of HEI nanocrystals in these three representative electrocatalytic reactions and aims to provide a basis for the rational design of next-generation multifunctional and high-performance catalysts.

Table 2. Representative electrocatalytic applications of HEI-based catalysts.

Synthetic Strategy	Composition	Structure	Electrocatalytic Application	Ref.
Thermally Driven HEA-to-HEI Conversion	PtPdAgFeCu	$L1_0$	HER	[55]
Arc-melting	FeCoNiAlTi	$L1_2$	HER	[60]
Thermally Driven HEA-to-HEI Conversion	$(IrRh)_2PrNdTb$	TCP	HER	[61]
Direct Thermally Driven Synthesis	$Pt_4FeCoNiCu$	$L1_0$	HER, ORR	[59]
Direct Thermally Driven Synthesis	PtFeCoNiCuZn	FCT	ORR	[29]
Direct Thermally Driven Synthesis	$Pt(FeCoNiCuZn)_3$	$L1_2$	ORR	[62]
Direct Thermally Driven Synthesis	PtCrFeCoNiZn	FCT	ORR	[33]
Direct Thermally Driven Synthesis	PtIrFeCoNiCu	FCC	ORR	[63]
Direct Thermally Driven Synthesis	$Pt(FeCoNiCu)_3$	$L1_2$	ORR	[64]
Direct Thermally Driven Synthesis	PtIrFeCoCu	$L1_0$	ORR	[30]
Direct Thermally Driven Synthesis	$Pt_4FeCoNiCu$, $Pt_5MnFeCoNiCu$	$L1_0$	ORR	[17]
Solution-phase synthesis	PdFeCoNiCu	$L1_2$	ORR	[65]
Thermally Driven HEA-to-HEI Conversion	$Pt_{0.45}Fe_{0.18}Co_{0.12}Ni_{0.15}Mn_{0.10}$	$L1_0$	ORR	[53]
Thermally Driven HEA-to-HEI Conversion	PtRhFeNiCu	FCC	EOR	[25]
Direct Thermally Driven Synthesis	PtPdAuFeCoNiCuSn	$L1_0$	EOR	[19]
Solution-phase synthesis	PtRhBiSnSb	HCP	EOR, Methanol oxidation reaction (MOR), Glycerol oxidation reaction (GOR)	[57]
Thermally Driven HEA-to-HEI Conversion	$(PtPdIrRu)_2FeCu$	$L1_0$	Formic acid oxidation reaction (FAOR)	[66]
Electrospinning	(PtIr)(FeMoBi)	$L1_0$	Ethylene glycol oxidation reaction (EGOR)	[67]
Solution-phase synthesis	$Pt_{0.8}Fe_{0.2}Co_{0.2}Ni_{0.2}Cu_{0.2}$ $Pt_{0.8}Fe_{0.2}Co_{0.2}Ni_{0.2}Zn_{0.2}$ $Pt_{0.8}Fe_{0.2}Co_{0.2}Ni_{0.2}Mn_{0.2}$	$L1_0$	Nitrate reduction reaction (NO_3^-RR)	[50]
Arc-melting	$(Fe_{0.25}Co_{0.25}Ni_{0.25}Cu_{0.25})_6Sn_5$	Monoclinic	NO_3^-RR	[68]
Direct Thermally Driven Synthesis	FeNiCuGaGe	BCC	Acetylene Semihydrogenation	[58]
Direct Thermally Driven Synthesis	(PtCoNi)(SnInGa)	Hexagonal NiAs-type	Propane dehydrogenation	[69]

4.1. Hydrogen Evolution Reaction (HER)

Amid the growing depletion of non-renewable energy resources, hydrogen has attracted increasing attention as a clean energy carrier with the potential to replace fossil fuels [70]. Among the various hydrogen-production technologies, the electrocatalytic HER is regarded as an efficient and sustainable route for large-scale hydrogen generation powered by renewable energy [71]. In acidic media, the HER process initiates with the Volmer step ($H^+ + e^- \rightarrow H^*$). H_2 is then released via either the Heyrovsky step ($H^+ + H^* + e^- \rightarrow H_2$) or the Tafel step ($H^* + H^* \rightarrow H_2$) [72]. According to the Sabatier principle [73], optimal activity requires moderate binding affinity: weak adsorption limits the Volmer step, while excessive binding hinders H_2 desorption. Thus, the hydrogen adsorption free energies (ΔG_{H^*}) ≈ 0 is the primary descriptor for peak performance, ensuring neither adsorption nor desorption becomes the rate-determining step (RDS) [73,74]. Unlike acidic systems, alkaline HER is fundamentally limited by sluggish water dissociation kinetics (the Volmer step), which imposes a high energy barrier for H-OH bond cleavage [75]. At low H* coverage, the reaction follows the Heyrovsky step ($H^* + H_2O + e^- \rightarrow H_2 + OH^-$), while high coverage favors the Tafel step ($H^* + H^* \rightarrow H_2$). Because of the additional water-dissociation barrier, even Pt shows HER activity in alkaline media that is several orders of magnitude lower than in acid. Nevertheless, alkaline electrolysis remains attractive for industrial applications because metallic electrodes generally exhibit better corrosion tolerance under alkaline conditions [76].

Owing to these intricate kinetic demands, traditional monometallic catalysts struggle to optimize the adsorption of multiple intermediates simultaneously. HEIs, characterized by their highly tunable electronic structures and multi-component synergistic effects, provide an ideal platform for the precise modulation of ΔG_{H^*} and hydroxide adsorption free energies (ΔG_{OH^*}). Saleem et al. reported PtPdAgFeCu HEI nanocrystals with an $L1_0$ intermetallic phase that exhibited excellent HER activity in 0.5 M H_2SO_4, with an overpotential of 24 mV at 10 mA cm^{-2}, a Tafel slope of 29 mV dec^{-1}, and a mass activity of 9.531 A mg_{Pt}^{-1} at −0.05 V vs. RHE, about 12 times higher than that of commercial Pt/C (Figure 12a–c) [55]. The catalyst also showed outstanding durability, retaining nearly 100% of its initial current density after 140 h at 100 mA cm^{-2} and 10000 CV cycles (Figure 12d,e). DFT calculations indicated that PtPdAgFeCu HEI nanocrystals possess a smaller absolute ΔG_{H^*} value, suggesting a more favorable HER environment (Figure 12f). The partial density of states (PDOS) analysis further reveals a high density of states for the Pt d-orbital near the Fermi level, which facilitates efficient charge transfer and enhances electrical conductivity (Figure 12g). Compared with pristine Pt, the redistribution of electronic states within the HEI lattice leads to a significant downshift of the d-band center. This electronic modulation effectively weakens the hydrogen binding affinity on the Pt surface, shifting the ΔG_{H^*} toward a near-thermoneutral value to boost HER kinetics.

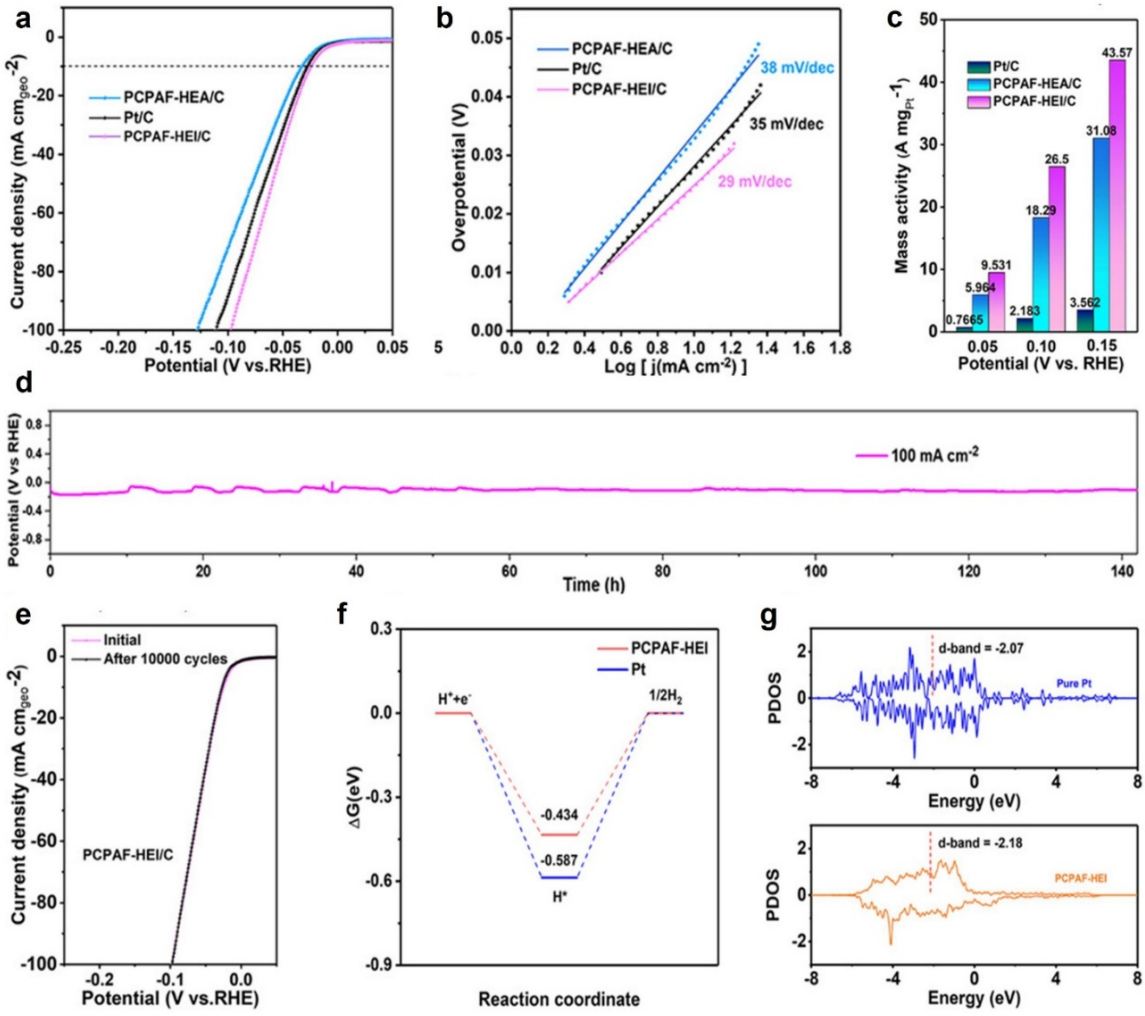

Figure 12. Electrocatalytic acidic HER performance of PtPdAgFeCu HEI nanocrystals in 0.5 M H_2SO_4. (**a**) HER polarization curves. (**b**) Tafel slopes. (**c**) Quantitative comparisons of HER mass activity. (**d**) Time-dependent overpotential curve at constant current density of 100 mA cm^{-2}. (**e**) Stability test recorded before and after 10000 cycles. (**f**) Calculated ΔG_{H^*} at the equilibrium potential. (**g**) PDOS of the d-band for the surface Pt atoms in the pure Pt (111) and HEI (111) slab system. Reproduced with permission [55]. Copyright 2024, John Wiley and Sons.

For alkaline HER, simultaneously optimizing the adsorption and desorption of OH* and H* on a single active site remains a major challenge [77]. To overcome this limitation, several high-performance catalysts have adopted dual-site strategies that separate the functions of water dissociation and hydrogen adsorption. These catalysts achieve superior activity by optimizing the synergistic balance between H_2O dissociation and the adsorbed hydrogen atom (H_{ad}) [78,79]. Building upon these principles, the multicomponent nature of HEI systems provides

a vast array of active sites and diverse configurations, enabling precise tuning of the adsorption strengths for various intermediate species. Wu et al. reported $(IrRh)_2PrNdTb$ HEI nanocrystals with a topologically close-packed (TCP) C15 structure [61]. Compared to disordered A1-$(IrRh)_2PrNdTb$ HEA nanocrystals and C15-Ir_2Pr, the resulting catalyst exhibited superior alkaline HER activity in 1 M KOH, which can be attributed to its larger ECSA and excellent intrinsic activity (Figure 13a,b). Besides, the HEI nanocrystals showed excellent stability with negligible degradation after a 200h stability test, confirming the high stability and minimal degradation of catalyst (Figure 13c). DFT calculations also demonstrate that the ΔG_{H^*} values of the HEI nanocrystals close to zero, indicating an optimal balance for hydrogen adsorption and desorption, which is essential for high catalytic efficiency (Figure 13d). Moreover, C15-$(IrRh)_2PrNdTb$ HEI nanocrystals exhibit stronger OH* binding energy, which facilitates the polarization and activation of adsorbed H_2O molecules, thereby accelerating the Volmer step (Figure 13e). The calculated water dissociation barriers of HEI nanocrystals exhibit lower values, ensuring a sufficient supply of active hydrogen during the Volmer step (Figure 13f). Figure 13g,h demonstrates that the strengthened *d-f* orbital coupling between noble metals (Ir, Rh) and rare earth elements (Pr, Nd, and Tb) in C15-$(IrRh)_2PrNdTb$ HEI nanocrystals not only facilitates water dissociation but also establishes a kinetically favorable hydrogen migration pathway, ensuring sufficient active hydrogen supply during the Volmer step.

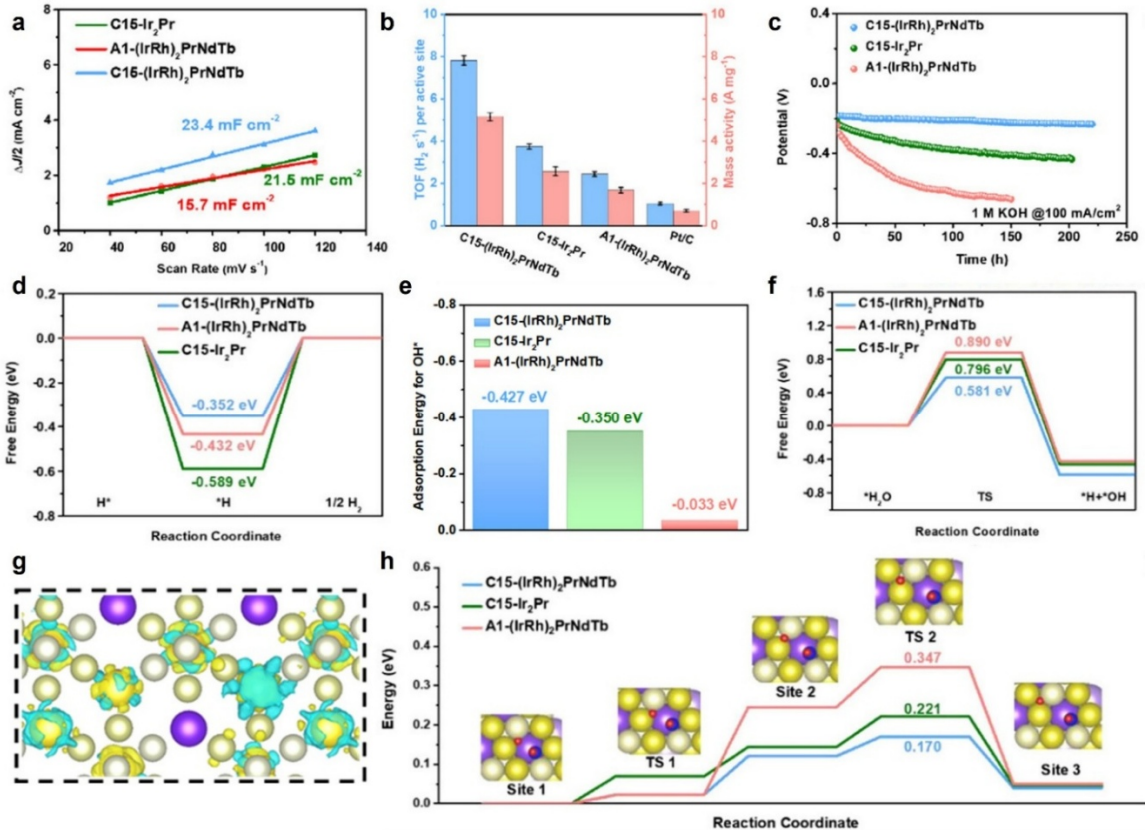

Figure 13. Electrocatalytic alkaline HER performance and theoretical analysis of C15-$(IrRh)_2PrNdTb$ HEI nanocrystals. (**a**) The double-layer capacitance (C_{dl}) curve. (**b**) The turnover frequency (TOF) values and mass activity. (**c**) Stability test recorded before and after 200h. (**d**) Calculated ΔG_{H^*} at the equilibrium potential. (**e**) Calculated ΔG_{OH^*} at the equilibrium potential. (**f**) The calculated energy barriers for water dissociation. (**g**) The difference charge density for C15-$(IrRh)_2PrNdTb$. (**h**) The kinetic energy barrier of the hydrogen spillover process. Reproduced with permission [61]. Copyright 2025, John Wiley and Sons.

Additionally, Huang et al. reported $Pt_4FeCoNiCu$ HEI nanocrystals with tunable degrees of chemical ordering [59]. In 1 M KOH, the highly ordered $Pt_4FeCoNiCu$ catalyst exhibited the best alkaline HER performance, requiring an overpotential of only 20 mV at 10 mA cm^{-2} and showing a Tafel slope of 31 mV dec^{-1} (Figure 14a). At a more practical potential of −0.2 V versus RHE, it delivered a mass activity of 71.9 A mg_{Pt}^{-1}, which is 2.1, 3.0, and 5.6 times higher than those of the partially ordered and disordered $Pt_4FeCoNiCu$ counterparts and commercial Pt/C, respectively (Figure 14b). These results clearly demonstrate that increasing the degree of ordering can substantially enhance alkaline HER kinetics. The improved activity is accompanied by markedly enhanced durability. Chronopotentiometry (CP) measurements showed that the highly ordered $Pt_4FeCoNiCu$ catalyst exhibited the smallest increase in potential during prolonged operation, indicating much slower deactivation than the partially

ordered, disordered, and Pt/C references (Figure 14c). This superior stability is further supported by the nearly overlapping HER polarization curves recorded before and after durability testing, confirming that the highly ordered catalyst retained its electrocatalytic performance with minimal degradation (Figure 14d). The ordering-dependent performance trend suggests that the chemically ordered intermetallic structure not only optimizes the electronic structure and adsorption behavior of reaction intermediates, but also enhances structural robustness under alkaline HER conditions. In this regard, stronger bonding within the ordered lattice and the higher thermodynamic stability of the intermetallic phase are likely key factors contributing to both the improved activity and long-term durability.

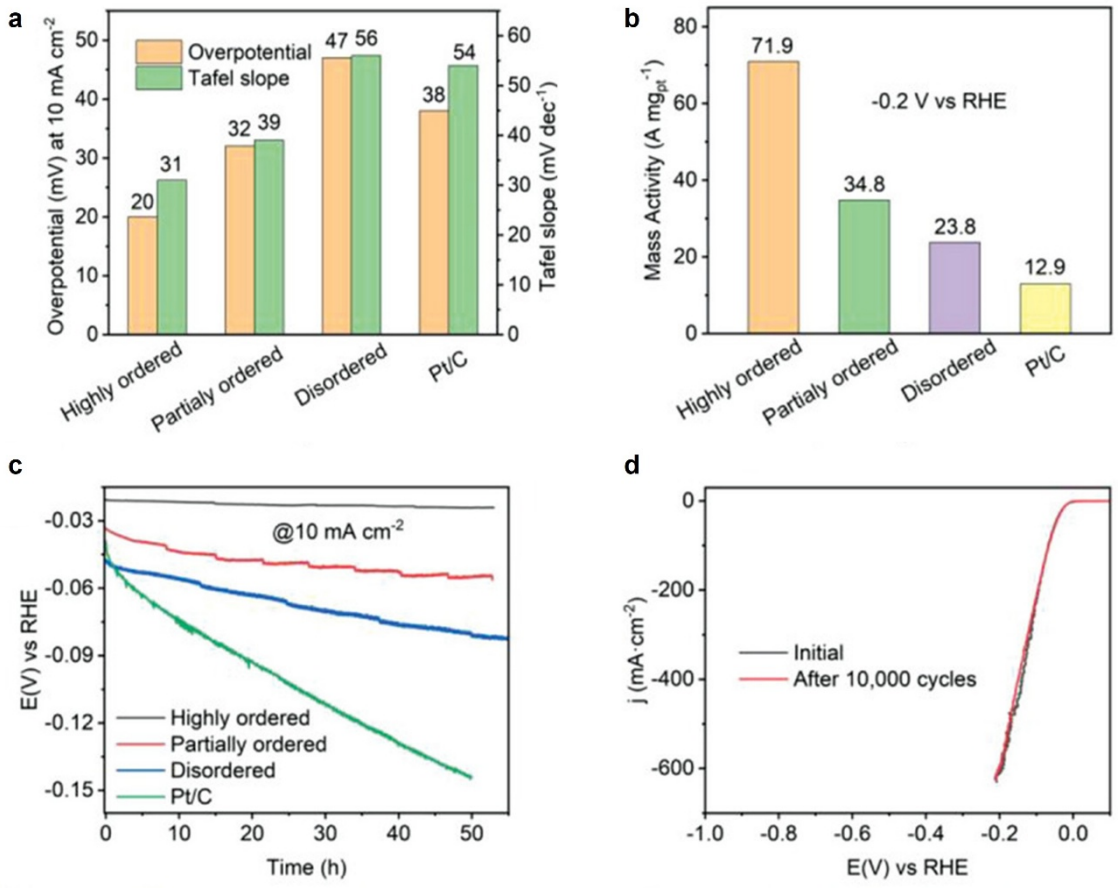

Figure 14. Electrocatalytic alkaline HER performance of $Pt_4FeCoNiCu$ HEI nanocrystals in 1 M KOH. (**a**) Overpotentials at 10 mA cm^{-2} and Tafel slopes of the catalysts. (**b**) HER mass activities of the catalysts. (**c**) CP curves of $Pt_4FeCoNiCu$ catalysts. (**d**) HER polarization curves of the highly ordered HEI catalyst before and after durability testing. Reproduced with permission [59]. Copyright 2023, John Wiley and Sons.

4.2. Oxygen Reduction Reaction (ORR)

The ORR is the key cathodic half-reaction in fuel cells and metal-air batteries, but its practical application is limited by large overpotentials and intrinsically sluggish kinetics arising from complex proton-coupled electron-transfer processes [80]. ORR generally proceeds through either a direct four-electron pathway that reduces O_2 to H_2O or an indirect two-electron pathway involving H_2O_2 as an intermediate [81]. Although Pt-based catalysts remain the benchmark because of their high activity and selectivity, their widespread application is hindered by high cost, limited abundance, and insufficient long-term durability [39,82]. These challenges highlight the need for more efficient, durable, and economically viable alternatives to conventional Pt-based catalysts. One promising strategy to address these limitations is to introduce non-noble metals into Pt-based systems to create HEI structures. Such multicomponent design not only reduces noble-metal usage but also broadens the compositional space, strengthens interatomic interactions, and enables more flexible tuning of electronic structure and adsorption behavior.

In this context, Xia et al. reported well-ordered PtFeCoNiCuZn HEI nanocrystals with a face-centered tetragonal (FCT) intermetallic structure, which exhibited excellent ORR performance in acidic media [29]. The PtFeCoNiCuZn HEI delivered a mass activity of 2.403 A mg_{Pt}^{-1} at 0.90 V versus RHE, which is approximately 19 times higher than that of commercial Pt/C (Figure 15a). Accelerated durability tests (ADTs) also showed that

the mass activity losses of PtFeCoNiCuZn HEI nanocrystals can be neglected after 10000 cycles of ADTs, indicating the high catalytic stability (Figure 15b). DFT calculations further revealed that the broadened d-band orbitals of the constituent elements enhance orbital overlap and interelement charge transfer, while also contributing to the generation of multiple catalytically active sites (Figure 15c–e). Furthermore, the charge density associated with the O-O bond in OOH at the Zn3 (Figure 15d) and Pt28 (Figure 15e) sites on the HEI (111) surface is significantly lower than that on Pt (111) (Figure 15c), indicating that the O-O bond can be more readily cleaved on the HEI surface. This suggests that the ordered multicomponent lattice creates a more favorable electronic environment for activating oxygenated intermediates and promoting the four-electron ORR pathway. This behavior is closely related to the modified electronic structure of the HEI catalyst. Because the electronic structure governs intermediate adsorption and reaction energetics, multielement incorporation and atomic ordering in PtFeCoNiCuZn broaden the d-band orbitals, enhance orbital overlap and charge transfer, and generate multiple active sites. As a result, both Pt and non-noble-metal sites can participate in ORR, leading to optimized adsorption behavior and improved catalytic kinetics. Building on this principle, Huang et al. demonstrated that highly ordered $L1_0$-Pt_4FeCoNiCu HEI nanocrystals have the best ORR mass activities than that of partially ordered HEAs, disordered HEAs, and Pt/C [59]. ADTs also proved that the highly ordered HEIs, characterized by increased configurational entropy, exhibit excellent ORR durability. These researches demonstrated that the ordered crystal structure with high entropy is more conducive to the selective exposure of active sites and the regulation of surface electronic structure, which significantly enhances the ORR catalytic activity.

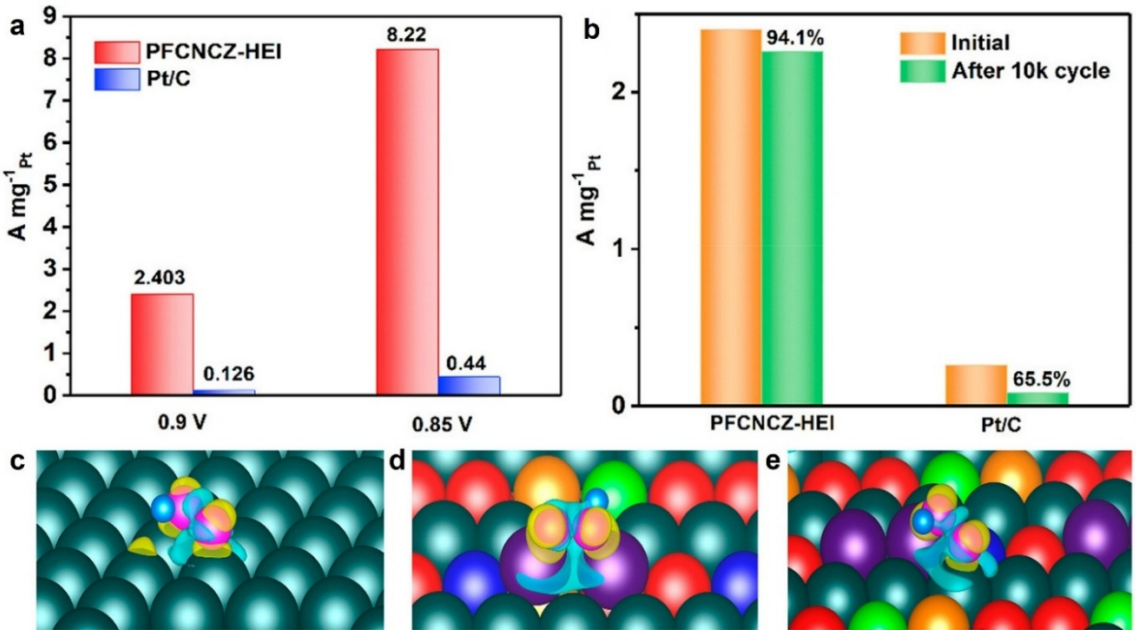

Figure 15. Electrocatalytic acidic ORR performance of PtFeCoNiCuZn HEI nanocrystals. (**a**) ORR mass activities of catalysts at 0.9 V vs RHE. (**b**) Mass activities before and after ADTs. Differential charge density of the OOH adsorbed system at (**c**) Pt (111), (**d**) the Zn3 site, and (**e**) the Pt28 site. Reproduced with permission [29]. Copyright 2023, American Chemical Society.

Furthermore, Luo et al. reported $L1_2$-ordered PdFeCoNiCu HEI nanocrystals, denoted as OHEA, which exhibited remarkable alkaline ORR activity with a high diffusion-limited current density (Figure 16a) [65]. At 0.9 V versus RHE, the OHEA catalyst delivered a mass activity of 2.037 mA μg_{Pd}^{-1}, which is substantially higher than those of disordered FCC PdFeCoNiCu HEA nanocrystals (DHEA) and commercial Pt/C (Figure 16b). In addition, OHEA showed a lower Tafel slope and superior durability, highlighting the beneficial effect of structural ordering on both ORR kinetics and stability. DFT calculations further revealed clear electronic-structure differences between OHEA and DHEA. In OHEA, the Co 3d orbitals are located closer to the Fermi level than in DHEA (Figure 16c,e), suggesting a more favorable electronic configuration for electrocatalytic electron transfer. Moreover, O_2 adsorption analysis showed evident orbital interaction between the catalyst and adsorbed oxygen on both materials, as reflected by the upshift of the O_2 s and p orbitals. Compared with DHEA, however, the Co 3d states in OHEA exhibit a more favorable shift near the Fermi level, which can facilitate electron transfer and stabilize adsorbed oxygen intermediates during ORR (Figure 16d, f). These results suggest that chemical ordering

not only modifies the electronic structure of HEI nanocrystals but also improves intermediate adsorption and charge-transfer behavior, thereby contributing to the enhanced alkaline ORR performance of OHEA.

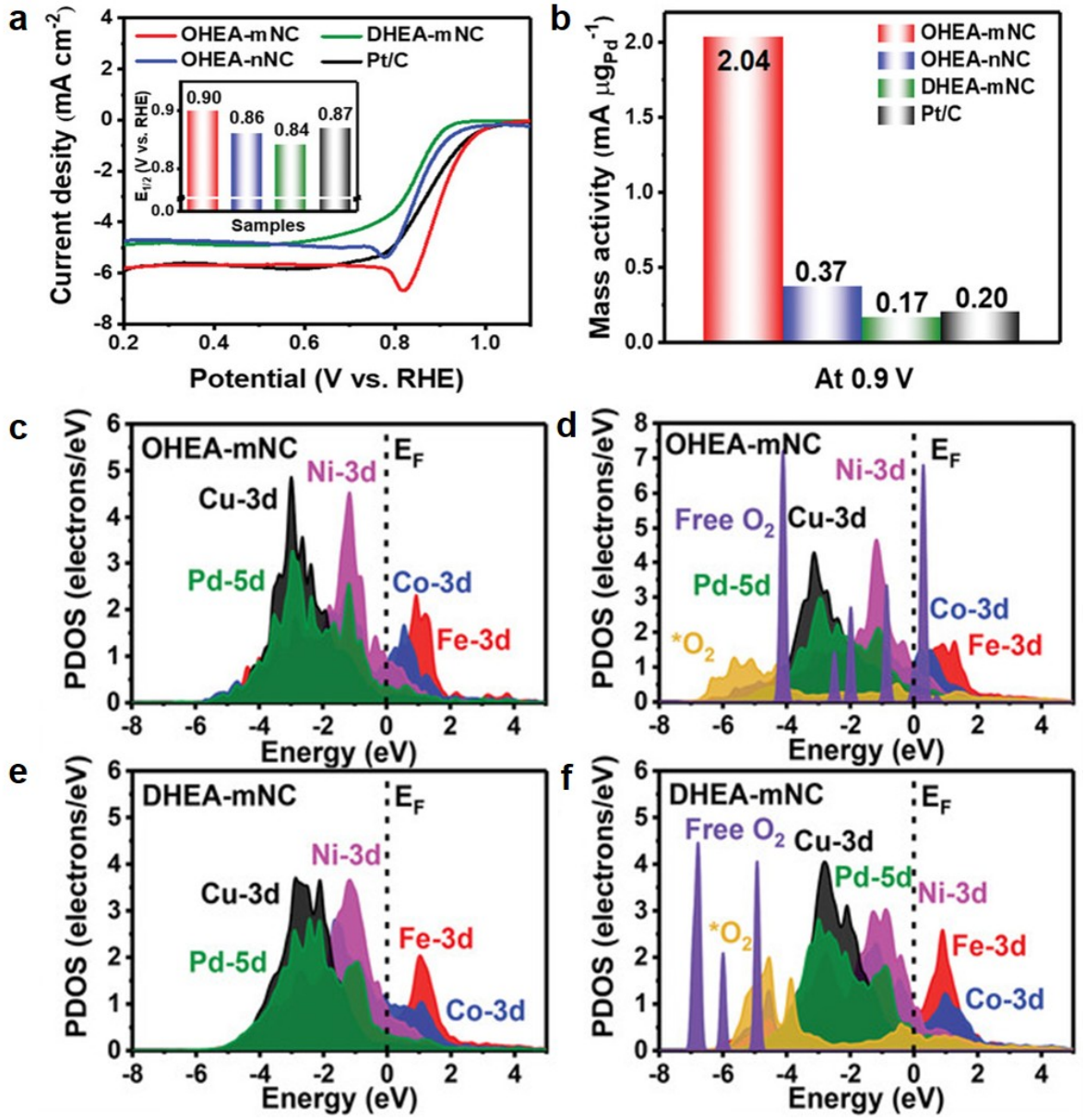

Figure 16. Electrocatalytic alkaline ORR performance of PdFeCoNiCu HEI nanocrystals. (**a**) Linear sweep voltammetry (LSV) curves. (**b**) Mass activities. (**c**,**e**) PDOSs of clean OHEA and DHEA, respectively. (**d**,**f**) PDOSs of O_2-adsorbed OHEA and DHEA, respectively. Reproduced with permission [65]. Copyright 2022, John Wiley and Sons.

4.3. Ethanol Oxidation Reaction (EOR)

The EOR is a representative anodic reaction in fuel cells, and ethanol is considered a promising liquid fuel because of its high energy density and ease of storage and handling. EOR can proceed through two major pathways [83]. The C1 pathway corresponds to complete oxidation of ethanol to CO_2, involving C-C bond cleavage and transfer of 12 electrons, and therefore enables maximal energy extraction. By contrast, the C2 pathway leads to incomplete oxidation products while preserving the C-C bond, which greatly limits the overall energy-conversion efficiency. In practice, most catalysts tend to favor the C2 pathway, and their performance is further compromised by sluggish C-C bond cleavage and poisoning from strongly adsorbed intermediates, especially CO. Therefore, a central challenge in EOR catalysis is to develop Pt-based catalysts with enhanced C-C bond-breaking ability, improved anti-poisoning capability, and higher overall activity [84].

In this context, Wang et al. reported structurally ordered FCC PtRhFeNiCu HEI nanocrystals that exhibited markedly improved EOR performance relative to the corresponding HEA nanocrystals and Pt/C [25]. The HEIs showed

higher mass activity, stronger CO tolerance, and superior durability, together with the lowest onset potential for CO removal among the compared catalysts. When used as the anode catalyst in a high-temperature polybenzimidazole-based direct ethanol fuel cell, the PtRhFeNiCu HEIs delivered a peak power density of 47.50 mW cm^{-2}, which is 2.97 times that of Pt/C (Figure 17a). More importantly, online gas chromatography revealed that the HEI nanocrystals generated the highest amount of C1 products, indicating a substantially enhanced ability to cleave the C-C bond and promote the complete oxidation pathway (Figure 17b). DFT calculations are further performed to clarify the origin of the superior EOR performance of the HEIs. The ordered HEI structure is thermodynamically more stable than the corresponding HEA structure (Figure 17c,d). In addition, the local density of states indicates that the d-band center of the HEIs is shifted farther away from the Fermi level than that of the HEAs, which helps weaken CO adsorption and thereby mitigate CO poisoning (Figure 17e). The calculated reaction-energy profiles further show that the HEIs exhibit a lower potential-limiting step for the electrochemical process and, more importantly, a substantially reduced energy barrier for C-C bond cleavage compared with the HEAs (Figure 17f,g). This result suggests that the ordered atomic arrangement of HEIs can facilitate both the electrochemical oxidation process and the key C-C bond-breaking step by altering the adsorption configuration of crucial intermediates.

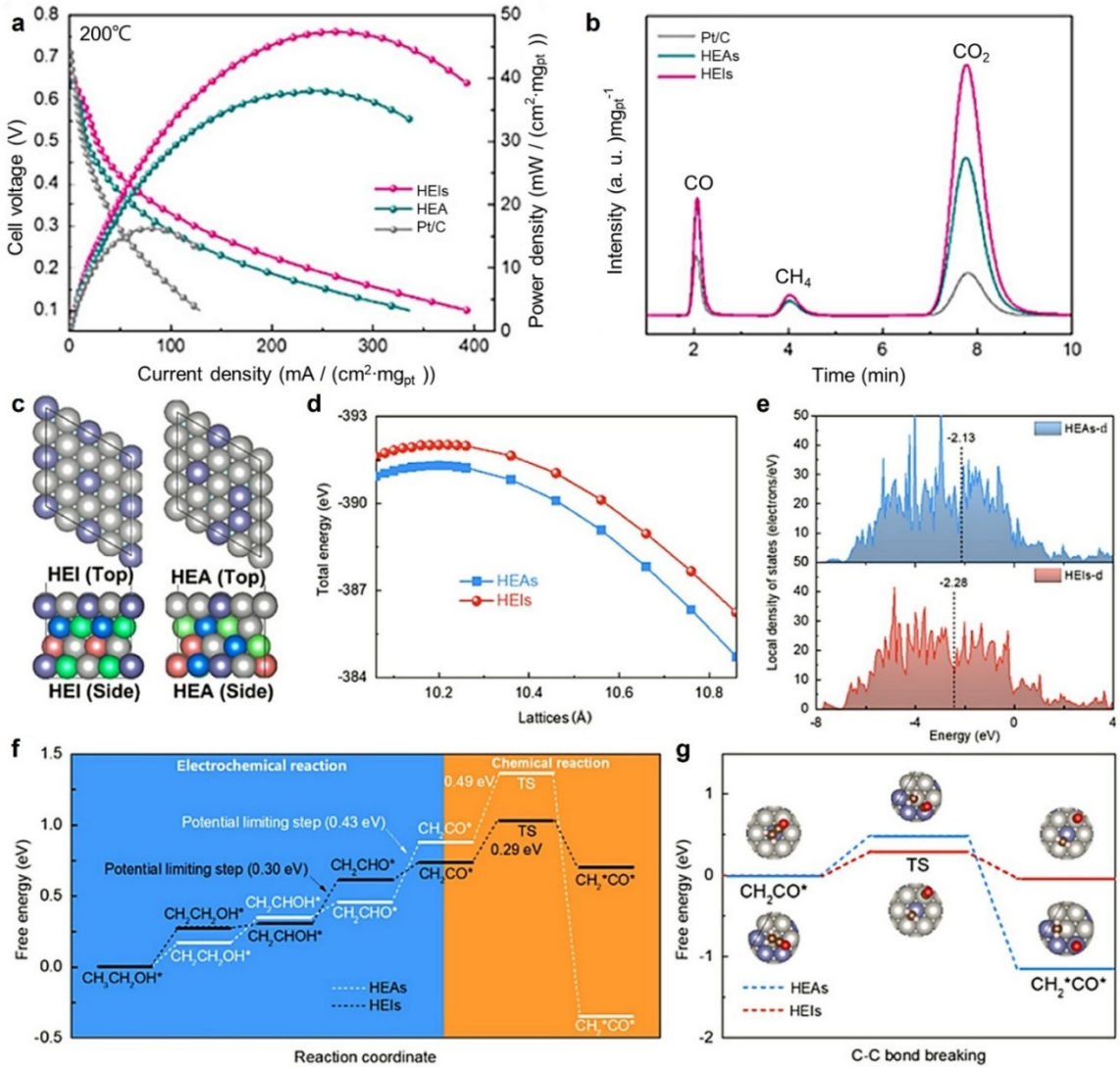

Figure 17. EOR performance and mechanistic analysis of PtRhFeNiCu HEI nanocrystals. (**a**) Polarization and power density curves obtained at 200 °C for the HEIs, HEAs, and Pt/C in a high-temperature polybenzimidazole-based direct ethanol fuel cell. (**b**) Gas-phase product distribution of ethanol electrooxidation measured by online gas chromatography. (**c**) Structural models of HEIs and HEAs viewed from the top and side. (**d**) Total energies of HEIs and HEAs with different lattice constants. (**e**) Local density of states of HEAs-d orbitals and HEIs-d orbitals. (**f**) Free-energy profiles of the EOR process on HEAs and HEIs, including electrochemical and chemical steps. (**g**) Energy barriers for C-C bond cleavage on HEAs and HEIs, together with the corresponding intermediate configuration. Reproduced with permission [25]. Copyright 2022, John Wiley and Sons.

5. Conclusions and Outlook

This review brings together recent progress in HEI nanocrystals, covering their formation principles, synthetic strategies, and electrocatalytic applications, and illustrates how atomic ordering and multicomponent complexity can be integrated within a single material platform. Compared with conventional disordered HEA nanocrystals and simpler intermetallic systems, HEI nanocrystals offer a distinctive opportunity to combine compositional diversity with structurally defined atomic arrangements, thereby creating new possibilities for regulating local coordination environments, heteroatomic interactions, and surface reactivity. In this Review, we have highlighted the thermodynamic and kinetic factors governing phase ordering in multicomponent nanoscale systems, summarized the key synthetic routes for accessing HEI nanocrystals with controlled structures, and discussed representative electrocatalytic applications in which structure, composition, and dynamic evolution jointly determine performance. We have also emphasized that the electrocatalytic advantages of HEI nanocrystals arise not only from their ordered frameworks, but also from the interplay between atomic occupation, surface structure, and reaction-dependent structural evolution. Taken together, these advances establish HEI nanocrystals as an emerging class of catalysts with considerable potential for achieving high activity, improved selectivity, and enhanced structural robustness.

Despite rapid progress in the development of HEI nanocrystals, the field remains at an early stage, and several key questions are still unresolved. In this regard, four critical directions are expected to shape future advances in the field.

5.1. Understanding the Growth Mechanisms of HEI Nanocrystals

A deeper understanding of the growth mechanisms of HEI nanocrystals is essential. Their formation often involves multiple precursors with distinct reduction potentials [22], which can lead to different reduction rates and thus increase the likelihood of phase separation, compositional heterogeneity, or kinetically trapped intermediates during synthesis. Beyond precursor conversion, the subsequent nucleation and growth processes may also involve extensive atomic diffusion and progressive structural transformation from disordered alloys to ordered intermetallic phases. A comprehensive understanding of these coupled processes is therefore required to reveal how composition, crystal phase, and atomic ordering evolve throughout synthesis. In particular, an important unresolved question is when and how atoms diffuse into specific crystallographic positions. It remains unclear whether preferred atomic occupation is established at the early nucleation stage, when the initial atomic framework is first created, or whether it mainly develops during later growth and post-growth rearrangement through thermally activated diffusion and ordering. Distinguishing between these possibilities is critical, because they imply fundamentally different synthetic control strategies. If atomic site occupation is largely determined during nucleation, then precursor conversion kinetics, local compositional fluctuations, and the earliest cluster structures may play a dominant role. By contrast, if ordering emerges primarily during growth or subsequent annealing, then diffusion barriers, interatomic interactions, and the balance between kinetic trapping and thermodynamic equilibration become more decisive.

This issue is further complicated by the fact that HEI nanocrystals contain multiple elements with different atomic sizes, bonding preferences, and mobilities. As a result, atomic diffusion is unlikely to occur uniformly across all elements, and some species may redistribute more readily than others during the transition from a disordered alloy to an ordered intermetallic structure. Understanding which elements migrate first, which atomic pairs preferentially form ordered motifs, and how these processes depend on temperature, particle size, and local chemical environment will be essential for clarifying the full growth pathway. Such insight would also help determine whether ordered HEI phases arise through direct nucleation of an ordered structure, through a disordered-to-ordered transformation during growth, or through post-synthetic atomic rearrangement after particle formation. In this regard, in situ characterization techniques will be particularly valuable. For example, in situ TEM [85] can track the evolution of particle size, morphology, composition, crystal phase, and structural ordering, while in situ spectroscopic methods such as XAS can provide complementary information on local coordination environments, oxidation states, and interatomic bonding [14,23]. When combined with time-resolved diffraction and theoretical modeling, these approaches can offer a more complete picture of the formation pathways of HEI nanocrystals. Ultimately, such mechanistic understanding will be essential for identifying how kinetic and thermodynamic parameters can be deliberately tuned to control precursor reduction, nucleation pathways, atomic diffusion, and final ordering behavior, thereby enabling the rational synthesis of HEI nanocrystals with targeted structures and properties.

5.2. Achieving Facet Control in HEI Nanocrystals

Facet control is critically important for catalysis because the exposed crystallographic planes determine the atomic arrangement, coordination environment, and electronic structure of active sites, thereby strongly influencing catalytic activity, selectivity, and durability. However, precise facet control in HEI nanocrystals remains highly challenging because of constraints arising from both thermodynamics and kinetics. Unlike simple alloys, HEIs require the simultaneous incorporation of five or more elements into a long-range ordered lattice, which greatly complicates surface and structural regulation. One major challenge is the thermodynamic instability of high-energy facets, which are prone to disappear during the high-temperature annealing typically required to drive the disorder-to-order transition. In addition, differences in the reduction potentials and reaction kinetics of multiple metal precursors often result in unbalanced deposition, phase separation, or loss of crystallographic uniformity, thereby hindering the formation of well-defined facets.

To address these challenges, several advanced synthetic strategies have been explored to regulate the surface structure of HEI nanocrystals. One effective approach is seed-mediated epitaxial growth combined with the dropwise addition of metal precursors, where preformed nanocrystal seeds with well-defined facets act as structural templates and the controlled precursor supply helps direct multicomponent deposition while preserving the desired symmetry [22,23,56,86–88]. Without such structural templates, facet control would need to rely more strongly on surface capping agents to direct crystal growth [89]. However, this remains particularly difficult in HEI systems because the chemically heterogeneous surface gives rise to highly complex ligand-surface interactions, and a single capping ligand rarely provides sufficiently selective and uniform adsorption across diverse atomic environments to stabilize a target crystallographic plane. In this regard, DFT calculations may serve as an important tool for screening and designing capping agents with appropriate facet-selective binding behavior for multicomponent HEI surfaces.

5.3. Probing Atomic-Scale Structures and Interatomic Interactions in HEI Nanocrystals

Atomic-scale characterization of HEI nanocrystals remains highly challenging because of their intrinsic structural and chemical complexity. Unlike conventional binary intermetallics, HEIs incorporate five or more principal elements into a long-range ordered lattice, generating highly heterogeneous local environments. Structural identification therefore requires not only verification of intermetallic ordering but also clarification of how multiple elements occupy specific atomic sites within individual nanocrystals. A major challenge is that conventional characterization techniques often lack sufficient sensitivity to resolve such local complexity. XRD mainly provides ensemble-averaged structural information and is therefore insufficient to distinguish local chemical ordering, site occupancy, or subtle compositional heterogeneity. Although HAADF-STEM offers much higher spatial resolution, direct identification of individual elements remains difficult when constituent atoms have similar atomic numbers. This limitation becomes even more severe in the presence of anti-site defects, vacancies, and local strain, making it difficult to determine whether the disorder-to-order transition occurs uniformly throughout the nanocrystal.

Elucidating interatomic interactions in HEIs is equally demanding. Their catalytic properties are governed by the coupled effects of local coordination, interatomic bonding, lattice distortion, and electronic structure modulation. In particular, the cocktail effect is often intertwined with local lattice distortion arising from atomic size mismatch and chemical heterogeneity, making it difficult to isolate the contribution of each factor. Future progress will require the integration of complementary methods that probe both local structure and electronic properties. XAS analysis, particularly EXAFS, can reveal local coordination environments and bond distances beyond the reach of diffraction methods. When combined with atomic-resolution electron microscopy, DFT calculations, and machine-learning-assisted simulations, these approaches can establish clearer correlations between local atomic configurations, electronic structure, and catalytic behavior, thereby guiding the rational design of HEI nanocrystals with optimized catalytic functionalities.

5.4. Elucidating Catalytic Mechanisms, Active Sites, and Interatomic Synergies in HEI Nanocrystals

Deciphering the catalytic mechanisms of HEI nanocrystals presents an unprecedented challenge due to the high configurational entropy and the vast diversity of potential adsorption sites on their surfaces. Unlike traditional catalysts with uniform active centers, the ordered yet multi-component nature of HEIs creates a complex “site-specific” landscape where the catalytic activity is governed by the precise atomic positions of five or more elements. A primary obstacle is the identification of the true active sites among countless possible atomic combinations (e.g., bridge, hollow, or top sites involving different metal neighbors). The structural ordering in HEIs imposes a sublattice constraint that creates unique coordination environments, yet the inherent chemical

randomness within these sublattices leads to a distribution of adsorption energies rather than a single value. This scaling relation break makes it difficult to pinpoint whether the observed activity stems from a specific high-symmetry site or from low-coordinated step sites and anti-site defects that are statistically prevalent in high-entropy systems.

Furthermore, probing the interatomic interactions that modulate these active sites requires sophisticated operando techniques to resolve how the electronic structure evolves during a reaction. The cocktail effect in HEIs implies that the adsorption strength of a reactant is not only determined by the atom it directly binds to but is also heavily tuned by the long-range electronic influence of neighboring atoms through orbital hybridization and charge redistribution. A major challenge is to decouple the geometric strain effect arising from atomic size mismatch from the ligand effect originating from electronic modulation at specific atomic positions. Future research must prioritize site-specific DFT simulations to resolve how local atomic configurations regulate catalytic behavior in HEI nanocrystals [90]. By mapping the d-band center shifts across different atomic coordinates, DFT calculations can help identify active site ensembles and clarify how synergistic interactions among diverse elements optimize the binding of reaction intermediates, ultimately providing a foundation for the rational design of HEI catalysts with superior atom-utilization efficiency.

Despite the rapid progress summarized in this Review, current HEI nanocrystals remain at an early stage with respect to practical and industrial implementation. Most reported synthetic methods still rely on precisely controlled rapid heating/quenching processes, thermally driven conversion, or solution-phase protocols, which are effective for mechanistic studies but remain difficult to translate into large-scale, reproducible production. In addition, although many HEI catalysts exhibit promising durability in laboratory-scale electrochemical tests, their long-term stability under realistic operating conditions, such as high current density, fluctuating potentials, and elevated temperatures, remains insufficiently evaluated. Another key consideration is the cost-performance balance, for which the intrinsic compositional diversity of HEI nanocrystals offers a distinct advantage by integrating noble metals with non-noble or earth-abundant elements in ordered multicomponent structures. Such noble-metal-diluted compositions can not only lower material cost but also create synergistic electronic, strain, and ensemble effects that contribute to enhanced activity and durability. Future studies should therefore place greater emphasis on quantitatively evaluating catalytic performance in relation to total catalyst cost, noble-metal content, mass loading, and device-level output, rather than relying only on activity normalized by geometric area or electrochemically active surface area. Addressing these challenges will be essential for moving HEI nanocrystals from proof-of-concept catalysts toward practically relevant catalytic materials.

Collectively, these four directions highlight the central challenges and opportunities that will define the next stage of HEI nanocrystal research. Future advances will rely on the tight integration of controllable synthesis, atomic-scale characterization, operando mechanistic analysis, and predictive theoretical modeling. By bridging these areas, researchers will be better positioned to uncover the fundamental principles governing atomic ordering, facet evolution, local electronic structure, and active site formation in HEIs. Such insight will provide a more rigorous foundation for the rational design of HEI nanocrystals with enhanced activity, selectivity, durability, and atom-utilization efficiency, ultimately broadening their impact in catalysis and sustainable energy technologies.

Author Contributions: T.-H.Y.: conceived and supervised the manuscript; C.-Y.W., B.-H.W. and T.-H.Y.: contributed to writing the manuscript. All authors have read and agreed to the published version of the manuscript.

Funding: This work is supported by the National Science and Technology Council, NSTC (112-2221-E-007-022-MY3, 113-2923-E-008-007, 114-2628-E-007-017, 114-2218-E-007-010, and 114-2224-E-007-001). This work is also financially supported by the "High Entropy Materials Center" from the Featured Areas Research Center Program within the framework of the Higher Education Sprout Project by the Ministry of Education (MOE) in Taiwan.

Data Availability Statement: Not applicable.

Conflicts of Interest: The authors declare no conflict of interest.

Use of AI and AI-Assisted Technologies: During the preparation of this work, the authors used ChatGPT (OpenAI) to assist in language editing and sentence polishing. No scientific content, data interpretation, or conclusions were generated by the tool. After using this tool, the authors reviewed and edited the content as needed and take full responsibility for the content of the published article.

References

1. Yeh, J.-W.; Chen, S.-K.; Lin, S.-J.; Gan, J.-Y.; Chin, T.-S.; Shun, T.-T.; Tsau, C.-H.; Chang, S.-Y. Nanostructured High-Entropy Alloys with Multiple Principal Elements: Novel Alloy Design Concepts and Outcomes. *Adv. Eng. Mater.* **2004**, *6*, 299–303.
2. Yao, Y.; Dong, Q.; Brozena, A.; Luo, J.; Miao, J.; Chi, M.; Wang, C.; Keverkidis, I.; Ren, Z.J.; Greeley, J.; et al. High-

Entropy Nanoparticles: Synthesis-Structure-Property Relationships and Data-Driven Discovery. *Science* **2022,** *376*, eabn3103.
3. Yeh, J.-W. Alloy Design Strategies and Future Trends in High-Entropy Alloys. *JOM* **2013**, *65*, 1759–1771.
4. Yao, Y.; Huang, Z.; Xie, P.; Lacey, S.D.; Jacob, R.J.; Xie, H.; Chen, F.; Nie, A.; Pu, T.; Rehwoldt, M.; et al. Carbothermal Shock Synthesis of High-Entropy-Alloy Nanoparticles. *Science* **2018**, *359*, 1489–1494.
5. Wang, X.; Dong, Q.; Qiao, H.; Huang, Z.; Saray, M.T.; Zhong, G.; Lin, Z.; Cui, M.; Brozena, A.; Hong, M.; et al. Continuous Synthesis of Hollow High-Entropy Nanoparticles for Energy and Catalysis Applications. *Adv. Mater.* **2020**, *32*, e2002853.
6. Wu, D.; Kusada, K.; Yamamoto, T.; Toriyama, T.; Matsumura, S.; Kawaguchi, S.; Kubota, Y.; Kitagawa, H. Platinum-Group-Metal High-Entropy-Alloy Nanoparticles. *J. Am. Chem. Soc.* **2020**, *142*, 13833–13838.
7. Sen, S.; Palabathuni, M.; Ryan, K.M.; Singh, S. High Entropy Oxides: Mapping the Landscape from Fundamentals to Future Vistas. *ACS Energy Lett.* **2024**, *9*, 3694–3718.
8. Hsu, W.-L.; Tsai, C.-W.; Yeh, A.-C.; Yeh, J.-W. Clarifying the Four Core Effects of High-Entropy Materials. *Nat. Rev. Chem.* **2024**, *8*, 471–485.
9. Zhao, M.; Wang, X.; Yang, X.; Gilroy, K.D.; Qin, D.; Xia, Y. Hollow Metal Nanocrystals with Ultrathin, Porous Walls and Well-Controlled Surface Structures. *Adv. Mater.* **2018**, *30*, e1801956.
10. Xia, Y.; Yang, X. Toward Cost-Effective and Sustainable Use of Precious Metals in Heterogeneous Catalysts. *Acc. Chem. Res.* **2017**, *50*, 450–454.
11. Li, H.; Lai, J.; Li, Z.; Wang, L. Multi-Sites Electrocatalysis in High-Entropy Alloys. *Adv. Funct. Mater.* **2021**, *31*, 2106715.
12. Gao, S.; Hao, S.; Huang, Z.; Yuan, Y.; Han, S.; Lei, L.; Zhang, X.; Shahbazian-Yassar, R.; Lu, J. Synthesis of High-Entropy Alloy Nanoparticles on Supports by the Fast Moving Bed Pyrolysis. *Nat. Commun.* **2020**, *11*, 2016.
13. Qiu, H.-J.; Fang, G.; Wen, Y.; Liu, P.; Xie, G.; Liu, X.; Sun, S. Nanoporous High-Entropy Alloys for Highly Stable and Efficient Catalysts. *J. Mater. Chem. A* **2019**, *7*, 6499–6506.
14. Feng, G.; Ning, F.; Song, J.; Shang, H.; Zhang, K.; Ding, Z.; Gao, P.; Chu, W.; Xia, D. Sub-2 nm Ultrasmall High-Entropy Alloy Nanoparticles for Extremely Superior Electrocatalytic Hydrogen Evolution. *J. Am. Chem. Soc.* **2021**, *143*, 17117–17127.
15. Zhan, C.; Xu, Y.; Bu, L.; Zhu, H.; Feng, Y.; Yang, T.; Zhang, Y.; Yang, Z.; Huang, B.; Shao, Q.; et al. Subnanometer High-Entropy Alloy Nanowires Enable Remarkable Hydrogen Oxidation Catalysis. *Nat. Commun.* **2021**, *12*, 6261.
16. Li, T.; Yao, Y.; Huang, Z.; Xie, P.; Liu, Z.; Yang, M.; Gao, J.; Zeng, K.; Brozena, A.H.; Pastel, G.; et al. Denary Oxide Nanoparticles as Highly Stable Catalysts for Methane Combustion. *Nat. Catal.* **2021**, *4*, 62–70.
17. Yang, C.-L.; Wang, L.-N.; Yin, P.; Liu, J.; Chen, M.-X.; Yan, Q.-Q.; Wang, Z.-S.; Xu, S.-L.; Chu, S.-Q.; Cui, C.; et al. Sulfur-Anchoring Synthesis of Platinum Intermetallic Nanoparticle Catalysts for Fuel Cells. *Science* **2021**, *374*, 459–464.
18. Mori, K.; Hashimoto, N.; Kamiuchi, N.; Yoshida, H.; Kobayashi, H.; Yamashita, H. Hydrogen Spillover-Driven Synthesis of High-Entropy Alloy Nanoparticles as a Robust Catalyst for CO_2 Hydrogenation. *Nat. Commun.* **2021**, *12*, 3884.
19. Cui, M.; Yang, C.; Huang, S.; Yang, M.; Overa, S.; Dong, Q.; Yao, Y.; Brozena, A.H.; Cullen, D.A.; Chi, M.; et al. Multi-Principal Element Intermetallic Nanoparticles Synthesized via a Disorder-to-Order Transition. *Sci. Adv.* **2022**, *8*, eabm4322.
20. Minamihara, H.; Kusada, K.; Wu, D.; Yamamoto, T.; Toriyama, T.; Matsumura, S.; Kumara, L.S.R.; Ohara, K.; Sakata, O.; Kawaguchi, S.; et al. Continuous-Flow Reactor Synthesis for Homogeneous 1 nm-Sized Extremely Small High-Entropy Alloy Nanoparticles. *J. Am. Chem. Soc.* **2022**, *144*, 11525–11529.
21. Gao, G.; Liang, J.; Guo, Z.; Yang, K.; Wang, G.; Wang, H.; Wan, X.; Li, Z.; Bai, Y.; Zhang, Y.; et al. Liquid Metal for High-Entropy Alloy Nanoparticles Synthesis. *Nature* **2023**, *619*, 73–77.
22. Liu, Y.-H.; Hsieh, C.-J.; Hsu, L.-C.; Lin, K.-H.; Hsiao, Y.-C.; Chi, C.-C.; Lin, J.-T.; Chang, C.-W.; Lin, S.-C.; Wu, C.-W.; et al. Toward Controllable and Predictable Synthesis of High-Entropy Alloy Nanocrystals. *Sci. Adv.* **2023**, *9*, eadf9931.
23. Hu, T.-H.; Wu, C.-Y.; He, Z.Y.; Chen, Y.; Hsu, L.-C.; Pao, C.-W.; Lin, J.-T.; Chang, C.-W.; Lin, S.-C.; Osmundsen, R.; et al. Unconventional Hexagonal Close-Packed High-Entropy Alloy Surfaces Synergistically Accelerate Alkaline Hydrogen Evolution. *Adv. Sci.* **2025**, *12*, e2409023.
24. KC, B.R.; Bastakoti, B.P. Rational Design of High-Entropy Materials for Photo and Electrocatalytic Applications. *Small Struct.* **2025**, *6*, 2500237.
25. Wang, D.; Chen, Z.; Wu, Y.; Huang, Y.-C.; Tao, L.; Chen, J.; Dong, C.-L.; Singh, C.V.; Wang, S. Structurally Ordered High-Entropy Intermetallic Nanoparticles with Enhanced C-C Bond Cleavage for Ethanol Oxidation. *SmartMat* **2023**, *4*, e1117.
26. Liu, J.; Lee, C.; Hu, Y.; Liang, Z.; Ji, R.; Soo, X.Y.D.; Zhu, Q.; Yan, Q. Recent Progress in Intermetallic Nanocrystals for Electrocatalysis: From Binary to Ternary to High-Entropy Intermetallics. *SmartMat* **2023**, *4*, e1210.
27. Liu, J.; Wang, X.; Singh, A.P.; Xu, H.; Kong, F.; Yang, F. The Evolution of Intermetallic Compounds in High-Entropy

Alloys: From the Secondary Phase to the Main Phase. *Metals* **2021**, *11*, 2054.
28. Soliman, S.S.; Dey, G.R.; McCormick, C.R.; Schaak, R.E. Temporal Evolution of Morphology, Composition, and Structure in the Formation of Colloidal High-Entropy Intermetallic Nanoparticles. *ACS Nano* **2023**, *17*, 16147–16159.
29. Chen, T.; Qiu, C.; Zhang, X.; Wang, H.; Song, J.; Zhang, K.; Yang, T.; Zuo, Y.; Yang, Y.; Gao, C.; et al. An Ultrasmall Ordered High-Entropy Intermetallic with Multiple Active Sites for the Oxygen Reduction Reaction. *J. Am. Chem. Soc.* **2024**, *146*, 1174–1184.
30. Feng, G.; Ning, F.; Pan, Y.; Chen, T.; Song, J.; Wang, Y.; Zou, R.; Su, D.; Xia, D. Engineering Structurally Ordered High-Entropy Intermetallic Nanoparticles with High-Activity Facets for Oxygen Reduction in Practical Fuel Cells. *J. Am. Chem. Soc.* **2023**, *145*, 11140–11150.
31. Soliman, S.S.; Eid, M.; Mitarotonda, Z.; MacIntosh, K.; McCormick, C.R.; Dey, G.R.; Schaak, R.E. Post-Synthetic Transformation of High-Entropy Alloy Nanoparticles into High-Entropy Intermetallics for Selective Acetylene Semi-Hydrogenation Catalysis. *J. Am. Chem. Soc.* **2025**, *147*, 23405–23415.
32. Ma, X.; Ma, C.; Wang, Y.-C.; Xia, J.; Han, S.; Zhang, H.; He, C.; Feng, F.; Lin, G.; Cao, W.; et al. Precise Control of Active Site Configurations in High-Entropy Intermetallic Compounds for Electrocatalytic Nitrate Reduction to Ammonia. *Angew. Chem. Int. Ed.* **2025**, *64*, e202502333.
33. Chen, T.; Zhang, X.; Wang, H.; Yuan, C.; Zuo, Y.; Gao, C.; Xiao, W.; Yu, Y.; Cai, J.; Luo, T.; et al. Antisite Defect Unleashes Catalytic Potential in High-Entropy Intermetallics for Oxygen Reduction Reaction. *Nat. Commun.* **2025**, *16*, 3308.
34. Han, S.Z.; Kang, J.; Kim, S.D.; Choi, S.Y.; Kim, H.G.; Lee, J.; Kim, K.; Lim, S.H.; Han, B. Reliable and Cost-Effective Design of Intermetallic Ni_2Si Nanowires and Direct Characterization of Its Mechanical Properties. *Sci. Rep.* **2015**, *5*, 15050.
35. Yang, Z.; Pedireddy, S.; Lee, H.K.; Tsuji, Y.; Chiu, C.-Y.; Huo, F.; Hng, H.H.; Yan, Q. Manipulating the d-Band Electronic Structure of Platinum-Functionalized Nanoporous Gold Bowls: Synergistic Intermetallic Interactions Enhance Catalysis. *Chem. Mater.* **2016**, *28*, 5080–5086.
36. Gamler, J.T.L.; Ashberry, H.M.; Skrabalak, S.E.; Koczkur, K.M. Random Alloyed versus Intermetallic Nanoparticles: A Comparison of Electrocatalytic Performance. *Adv. Mater.* **2018**, *30*, e1801563.
37. Li, J.; Sun, S. Intermetallic Nanoparticles: Synthetic Control and Their Enhanced Electrocatalysis. *Acc. Chem. Res.* **2019**, *52*, 2015–2025.
38. Yan, Y.; Du, J.S.; Gilroy, K.D.; Yang, D.; Xia, Y.; Zhang, H. Intermetallic Nanocrystals: Syntheses and Catalytic Applications. *Adv. Mater.* **2017**, *29*, 1605997.
39. Zhou, M.; Li, C.; Fang, J. Noble-Metal-Based Random Alloy and Intermetallic Nanocrystals: Syntheses and Applications. *Chem. Rev.* **2021**, *121*, 736–795.
40. Cui, M.; Yang, C.; Hwang, S.; Li, B.; Dong, Q.; Wu, M.; Xie, H.; Wang, X.; Wang, G.; Hu, L. Rapid Atomic Ordering Transformation toward Intermetallic Nanoparticles. *Nano Lett.* **2022**, *22*, 255–262.
41. Chen, X.; Zhang, S.; Li, C.; Liu, Z.; Sun, X.; Cheng, S.; Zakharov, D.N.; Hwang, S.; Zhu, Y.; Fang, J.; et al. Composition-Dependent Ordering Transformations in Pt-Fe Nanoalloys. *Proc. Natl. Acad. Sci. USA* **2022**, *119*, e2117899119.
42. Ma, T.; Wang, S.; Chen, M.; Maligal-Ganesh, R.V.; Wang, L.-L.; Johnson, D.D.; Kramer, M.J.; Huang, W.; Zhou, L. Toward Phase and Catalysis Control: Tracking the Formation of Intermetallic Nanoparticles at Atomic Scale. *Chem* **2019**, *5*, 1235–1247.
43. Li, F.; Zong, Y.; Ma, Y.; Wang, M.; Shang, W.; Tao, P.; Song, C.; Deng, T.; Zhu, H.; Wu, J. Atomistic Imaging of Competition between Surface Diffusion and Phase Transition during the Intermetallic Formation of Faceted Particles. *ACS Nano* **2021**, *15*, 5284–5293.
44. Guo, J.; Liu, W.; Fu, X.; Jiao, S. Wet-Chemistry Synthesis of Two-Dimensional Pt- and Pd-Based Intermetallic Electrocatalysts for Fuel Cells. *Nanoscale* **2023**, *15*, 8508–8531.
45. Gao, Q.; Yao, B.; Pillai, H.S.; Zang, W.; Han, X.; Liu, Y.; Yu, S.-W.; Yan, Z.; Min, B.; Zhang, S.; et al. Synthesis of Core/Shell Nanocrystals with Ordered Intermetallic Single-Atom Alloy Layers for Nitrate Electroreduction to Ammonia. *Nat. Synth.* **2023**, *2*, 624–634.
46. Han, S.; Sun, H.; Ma, C.; Yun, Q.; He, C.; Ma, X.; Zhang, H.; Feng, F.; Meng, X.; Xia, J.; et al. Wet-Chemical Epitaxial Growth of Metastable-Phase Intermetallic Electrocatalysts. *Adv. Funct. Mater.* **2024**, *34*, 2403023.
47. Rößner, L.; Armbrüster, M. Electrochemical Energy Conversion on Intermetallic Compounds: A Review. *ACS Catal.* **2019**, *9*, 2018–2062.
48. Nie, Z.; Li, Y.; Zhang, X.; Chen, T.; Wang, H.; Song, J.; Yang, T.; Zuo, Y.; Gao, C.; Xiao, W.; et al. Tailoring the d-Band Center by Intermetallic Charge-Transfer Manipulation in Bimetal Alloy Nanoparticle Confined in N-Doped Carbon Nanobox for Efficient Rechargeable Zn-Air Battery. *Chem. Eng. J.* **2023**, *463*, 142411.
49. Qi, Z.; Xiao, C.; Liu, C.; Goh, T.W.; Zhou, L.; Maligal-Ganesh, R.V.; Pei, Y.; Li, X.; Curtiss, L.A.; Huang, W. Sub-4 nm PtZn Intermetallic Nanoparticles for Enhanced Mass and Specific Activities in Catalytic Electrooxidation Reaction. *J. Am. Chem. Soc.* **2017**, *139*, 4762–4768.
50. Zhu, G.; Bao, W.; Xie, M.; Qi, C.; Xu, F.; Jiang, Y.; Chen, B.; Fan, Y.; Liu, B.; Wang, L.; et al. Accelerating Tandem

Electroreduction of Nitrate to Ammonia via Multi-Site Synergy in Mesoporous Carbon-Supported High-Entropy Intermetallics. *Adv. Mater.* **2025**, *37*, e2413560.

51. Kar, N.; Leonardi, A.; McCoy, M.; Selvaraj, R.; Skrabalak, S.E. A Programmable Nanoparticle Conversion Pathway to Monodisperse Polyelemental High-Entropy Alloy, Intermetallic, and Multiphase Nanoparticles. *Angew. Chem. Int. Ed.* **2025**, *64*, e202505523.
52. Chen, T.; Wang, Y.; Liu, W.; Liu, K.; Xia, D. Nano-Engineered High-Entropy Intermetallic Compounds for Catalysis: From Designs to Catalytic Applications. *Electrochem. Energy Rev.* **2025**, *8*, 30.
53. Hu, Y.; Xu, Z.; Guo, X.; Xiong, P.; Xu, C.; Chen, C.; Zhang, Q.; Wang, S.; Wu, T.-S.; Soo, Y.-L.; et al. Hollow-Carbon Confinement Annealing: A New Synthetic Approach to Make High-Entropy Solid-Solution and Intermetallic Nanoparticles. *Nano Lett.* **2023**, *23*, 10765–10771.
54. Schlegel, N.; Punke, S.; Clausen, C.M.; Friis-Jensen, U.; Johansen, F.L.; Anker, A.S.; Jensen, K.M.Ø. Tracking the Formation of High-Entropy Solid Solutions and High-Entropy Intermetallics by In Situ X-ray Diffraction and Spectroscopy. *Chem. Mater.* **2025**, *37*, 939–953.
55. Zheng, S.; Zhang, H.; Liu, C.; Wang, X.; Huang, Y.; Huo, F. Ultrathin Template Approach to Synthesize High-Entropy Intermetallic Nanoparticles for Hydrogen Evolution Reaction. *Small Struct.* **2024**, *5*, 2300537.
56. Wu, C.-Y.; Hsiao, Y.-C.; Chen, Y.; Lin, K.-H.; Lee, T.-J.; Chi, C.-C.; Lin, J.-T.; Hsu, L.-C.; Tsai, H.-J.; Gao, J.-Q.; et al. A Catalyst Family of High-Entropy Alloy Atomic Layers with Square Atomic Arrangements Comprising Iron- and Platinum-Group Metals. *Sci. Adv.* **2024**, *10*, eadl3693.
57. Chen, W.; Luo, S.; Sun, M.; Wu, X.; Zhou, Y.; Liao, Y.; Tang, M.; Fan, X.; Huang, B.; Quan, Z. High-Entropy Intermetallic PtRhBiSnSb Nanoplates for Highly Efficient Alcohol Oxidation Electrocatalysis. *Adv. Mater.* **2022**, *34*, 2206276.
58. Ma, J.; Xing, F.; Nakaya, Y.; Shimizu, K.-i.; Furukawa, S. Nickel-Based High-Entropy Intermetallic as a Highly Active and Selective Catalyst for Acetylene Semihydrogenation. *Angew. Chem. Int. Ed.* **2022**, *61*, e202200889.
59. Wang, Y.; Gong, N.; Liu, H.; Ma, W.; Hippalgaonkar, K.; Liu, Z.; Huang, Y. Ordering-Dependent Hydrogen Evolution and Oxygen Reduction Electrocatalysis of High-Entropy Intermetallic $Pt_4FeCoCuNi$. *Adv. Mater.* **2023**, *35*, 2302067.
60. Jia, Z.; Yang, T.; Sun, L.; Zhao, Y.; Li, W.; Luan, J.; Lyu, F.; Zhang, L.-C.; Kruzic, J.J.; Kai, J.-J.; et al. A Novel Multinary Intermetallic as an Active Electrocatalyst for Hydrogen Evolution. *Adv. Mater.* **2020**, *32*, 2000385.
61. Wu, Q.; Li, Y.; Cao, Y.; Li, J.; Mao, J.; Liu, X.; Qu, W.; Yan, P.; Cai, Z.; Lv, H.; et al. High-Entropy Topologically Close-Packed Ir Alloys Enable Interatomic Hydrogen Spillover for Hydrogen Evolution toward High-Performing Anion Exchange Membrane Water Electrolyzers. *Angew. Chem. Int. Ed.* **2026**, *65*, e17120.
62. Zhang, Q.; Shen, T.; Song, M.; Wang, S.; Zhang, J.; Huang, X.; Lu, S.; Wang, D. High-Entropy $L1_2$-$Pt(FeCoNiCuZn)_3$ Intermetallics for Ultrastable Oxygen Reduction Reaction. *J. Energy Chem.* **2023**, *86*, 158–166.
63. Jiang, Y.; Zhang, Q.; Sun, J.; Xiao, C.; Zhao, T.; Zeng, L. Revealing Robust Atomic Configurations of the Ligand-Assisted Synthesized High-Entropy PtIrFeCoNiCu Nano-Intermetallic Catalysts During Oxygen Reductions in Fuel Cells. *Adv. Sci.* **2026**, *13*, e17892.
64. Zhang, L.; Zhang, X.; Chen, C.; Zhang, J.; Tan, W.; Xu, Z.; Zhong, Z.; Du, L.; Song, H.; Liao, S.; et al. Machine Learning-Aided Discovery of Low-Pt High Entropy Intermetallic Compounds for Electrochemical Oxygen Reduction Reaction. *Angew. Chem. Int. Ed.* **2024**, *63*, e202411123.
65. Zhu, G.; Jiang, Y.; Yang, H.; Wang, H.; Fang, Y.; Wang, L.; Xie, M.; Qiu, P.; Luo, W. Constructing Structurally Ordered High-Entropy Alloy Nanoparticles on Nitrogen-Rich Mesoporous Carbon Nanosheets for High-Performance Oxygen Reduction. *Adv. Mater.* **2022**, *34*, 2110128.
66. Shen, T.; Xiao, D.; Deng, Z.; Wang, S.; An, L.; Song, M.; Zhang, Q.; Zhao, T.; Gong, M.; Wang, D. Stabilizing Diluted Active Sites of Ultrasmall High-Entropy Intermetallics for Efficient Formic Acid Electrooxidation. *Angew. Chem. Int. Ed.* **2024**, *63*, e202403260.
67. Hao, J.; Wang, T.; Cai, J.; Gao, G.; Zhuang, Z.; Yu, R.; Wu, J.; Wu, G.; Lu, S.; Wang, X.; et al. Suppression of Structural Heterogeneity in High-Entropy Intermetallics for Electrocatalytic Upgrading of Waste Plastics. *Angew. Chem. Int. Ed.* **2025**, *64*, e202419369.
68. Xiang, Z.; Lu, Y.-R.; Meng, L.; Lan, J.; Xie, F.; Gao, S.; Li, J.; Luo, M.; Peng, M.; Tan, Y. Active Hydrogen Enrichment on Cu_6Sn_5-type High Entropy Intermetallics for Efficient Nitrate Reduction Reaction. *Adv. Mater.* **2025**, *37*, 2501886.
69. Xing, F.; Ma, J.; Shimizu, K.-i.; Furukawa, S. High-Entropy Intermetallics on Ceria as Efficient Catalysts for the Oxidative Dehydrogenation of Propane Using CO_2. *Nat. Commun.* **2022**, *13*, 5065.
70. Xu, Y.; Wang, C.; Huang, Y.; Fu, J. Recent Advances in Electrocatalysts for Neutral and Large-Current-Density Water Electrolysis. *Nano Energy* **2021**, *80*, 105545.
71. Zhang, H.; Cheng, C.; Zhou, J.; Ma, C.; Shi, P.; Wu, H.; Yin, P.; Cao, W.; Xia, J.; Zhu, L.; et al. Atomically Dispersed Ruthenium Sites with Electron-Rich Environments in Intermetallic Compounds for High-Current-Density Hydrogen Evolution. *J. Mater. Chem. A* **2023**, *11*, 10328–10336.

72. Ren, J.-T.; Chen, L.; Wang, H.-Y.; Yuan, Z.-Y. High-Entropy Alloys in Electrocatalysis: From Fundamentals to Applications. *Chem. Soc. Rev.* **2023**, *52*, 8319–8373.
73. Huang, Y.-M.; Chang, C.-W.; Lin, J.-T.; He, Z.-Y.; Chen, Y.; Chang, H.-S.; Lin, S.-C.; Liu, H.-Y.; Tsai, Y.-S.; Lee, S.-C.; et al. Toward the Sabatier Principle-Guided Design of Low-Platinum-Group-Metal Trimetallic Nanocatalysts for Efficient Hydrogen Evolution and Oxidation Reactions. *Adv. Funct. Mater.* **2026**, *36*, e14858.
74. Rao, C.N.R.; Chhetri, M. Borocarbonitrides as Metal-Free Catalysts for the Hydrogen Evolution Reaction. *Adv. Mater.* **2019**, *31*, 1803668.
75. Morales-Guio, C.G.; Stern, L.-A.; Hu, X. Nanostructured Hydrotreating Catalysts for Electrochemical Hydrogen Evolution. *Chem. Soc. Rev.* **2014**, *43*, 6555–6569.
76. Gao, G.; Zhu, G.; Chen, X.; Sun, Z.; Cabot, A. Optimizing Pt-Based Alloy Electrocatalysts for Improved Hydrogen Evolution Performance in Alkaline Electrolytes: A Comprehensive Review. *ACS Nano* **2023**, *17*, 20804–20824.
77. Wang, X.; Zheng, Y.; Sheng, W.; Xu, Z.J.; Jaroniec, M.; Qiao, S.-Z. Strategies for Design of Electrocatalysts for Hydrogen Evolution under Alkaline Conditions. *Mater. Today* **2020**, *36*, 125–138.
78. Jin, H.; Liu, X.; Jiao, Y.; Vasileff, A.; Zheng, Y.; Qiao, S.-Z. Constructing Tunable Dual Active Sites on Two-Dimensional C_3N_4@MoN Hybrid for Electrocatalytic Hydrogen Evolution. *Nano Energy* **2018**, *53*, 690–697.
79. Oh, A.; Sa, Y.J.; Hwang, H.; Baik, H.; Kim, J.; Kim, B.; Joo, S.H.; Lee, K. Rational Design of Pt-Ni-Co Ternary Alloy Nanoframe Crystals as Highly Efficient Catalysts Toward the Alkaline Hydrogen Evolution Reaction. *Nanoscale* **2016**, *8*, 16379–16386.
80. Cui, P.; Zhao, L.; Long, Y.; Dai, L.; Hu, C. Carbon-Based Electrocatalysts for Acidic Oxygen Reduction Reaction. *Angew. Chem. Int. Ed.* **2023**, *62*, e202218269.
81. Sun, Y.; Han, L.; Strasser, P. A Comparative Perspective of Electrochemical and Photochemical Approaches for Catalytic H_2O_2 Production. *Chem. Soc. Rev.* **2020**, *49*, 6605–6631.
82. Du, L.; Prabhakaran, V.; Xie, X.; Park, S.; Wang, Y.; Shao, Y. Low-PGM and PGM-Free Catalysts for Proton Exchange Membrane Fuel Cells: Stability Challenges and Material Solutions. *Adv. Mater.* **2021**, *33*, 1908232.
83. Sun, H.; Li, L.; Chen, Y.; Kim, H.; Xu, X.; Guan, D.; Hu, Z.; Zhang, L.; Shao, Z.; Jung, W. Boosting Ethanol Oxidation by NiOOH-CuO Nano-Heterostructure for Energy-Saving Hydrogen Production and Biomass Upgrading. *Appl. Catal. B* **2023**, *325*, 122388.
84. Zhu, Y.; Bu, L.; Shao, Q.; Huang, X. Subnanometer PtRh Nanowire with Alleviated Poisoning Effect and Enhanced C-C Bond Cleavage for Ethanol Oxidation Electrocatalysis. *ACS Catal.* **2019**, *9*, 6607–6612.
85. Tamadoni Saray, M.; Yurkiv, V.R.; Shahbazian-Yassar, R. In Situ TEM Studies on the Formation of High-Entropy Alloy Nanoparticles from Mixed Metal-Salt Precursors. *Langmuir* **2025**, *41*, 14727–14742.
86. Hsiao, Y.-C.; Wu, C.-Y.; Lee, C.-H.; Huang, W.-Y.; Thang, H.V.; Chi, C.-C.; Zeng, W.-J.; Gao, J.-Q.; Lin, C.-Y.; Lin, J.-T.; et al. A Library of Seed@High-Entropy-Alloy Core-shell Nanocrystals With Controlled Facets for Catalysis. *Adv. Mater.* **2025**, *37*, 2411464.
87. Fang, H.-W.; Hou, L.-Y.; Chi, C.-C.; Wu, C.-Y.; Wu, C.-Y.; Chang, C.-W.; Lin, J.-T.; Lin, S.-C.; He, Z.Y.; Chen, Y.; et al. High-Index Faceted High-Entropy-Alloy Atomic Layers with Tailored Active Sites for Enhanced Catalytic Performance. *Mater. Today* **2026**, *93*, 103195.
88. Lin, C.-Y.; He, Z.Y.; Lin, J.-T.; Chang, C.-W.; Hsiao, Y.-C.; Lin, S.-C.; Chen, Y.; Huang, Y.-M.; Lee, S.-C.; Pao, C.-W.; et al. Atomically Mixed High-Entropy-Alloy Nanoframes with 3D Subnanometer-Thick Electrocatalytic Surfaces. *Adv. Funct. Mater.* **2025**, *35*, 2505927.
89. Yang, T.-H.; Shi, Y.; Janssen, A.; Xia, Y. Surface Capping Agents and Their Roles in Shape-Controlled Synthesis of Colloidal Metal Nanocrystals. *Angew. Chem. Int. Ed.* **2020**, *59*, 15378–15401.
90. Chen, Z.W.; Li, J.; Ou, P.; Huang, J.E.; Wen, Z.; Chen, L.; Yao, X.; Cai, G.; Yang, C.C.; Singh, C.V.; et al. Unusual Sabatier Principle on High Entropy Alloy Catalysts for Hydrogen Evolution Reactions. *Nat. Commun.* **2024**, *15*, 359.